Acta Pharmaceutica Sinica B 2022;12(6):2710–2730

Chinese Pharmaceutical Association
Institute of Materia Medica, Chinese Academy of Medical Sciences

Acta Pharmaceutica Sinica B

www.elsevier.com/locate/apsb
www.sciencedirect.com

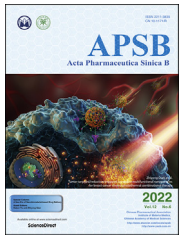

ORIGINAL ARTICLE

Tumor-targeted/reduction-triggered composite multifunctional nanoparticles for breast cancer chemo-photothermal combinational therapy

Yun Yang[a], Danrong Hu[a], Yi Lu[b], Bingyang Chu[a], Xinlong He[a], Yu Chen[a], Yao Xiao[a], Chengli Yang[a], Kai Zhou[a], Liping Yuan[a], Zhiyong Qian[a,*]

[a]*State Key Laboratory of Biotherapy and Cancer Center, West China Hospital, Sichuan University, Collaborative Innovation Center of Biotherapy, Chengdu 610041, China*
[b]*West China School of Pharmacy, Sichuan University, Chengdu 610041, China*

Received 24 May 2021; received in revised form 9 July 2021; accepted 2 August 2021

KEY WORDS

Breast cancer;
Chem-photothermal combinational therapy;
Camptothecin;
Prussian blue nanoparticles;
Reduction-responsive prodrugs

Abstract Breast cancer has become the most commonly diagnosed cancer type in the world. A combination of chemotherapy and photothermal therapy (PTT) has emerged as a promising strategy for breast cancer therapy. However, the intricacy of precise delivery and the ability to initiate drug release in specific tumor sites remains a challenging puzzle. Therefore, to ensure that the therapeutic agents are synchronously delivered to the tumor site for their synergistic effect, a multifunctional nanoparticle system (PCRHNs) is developed, which is grafted onto the prussian blue nanoparticles (PB NPs) by reduction-responsive camptothecin (CPT) prodrug copolymer, and then modified with tumor-targeting peptide cyclo(Asp-D-Phe-Lys-Arg-Gly) (cRGD) and hyaluronic acid (HA). PCRHNs exhibited nano-sized structure with good monodispersity, high load efficiency of CPT, triggered CPT release in response to reduction environment, and excellent photothermal conversion under laser irradiation. Furthermore, PCRHNs can act as a photoacoustic imaging contrast agent-guided PTT. *In vivo* studies indicate that PCRHNs exhibited excellent biocompatibility, prolonged blood circulation, enhanced tumor accumulation, allow tumor-specific chemo-photothermal therapy to achieve synergistic antitumor effects with reduced systemic toxicity. Moreover, hyperthermia-induced upregulation of heat shock protein 70 in the tumor cells could be inhibited by CPT. Collectively, PCRHNs may be a promising therapeutic way for breast cancer therapy.

*Corresponding author. Tel./fax: +86 28 85557632.
E-mail address: zhiyongqian@scu.edu.cn (Zhiyong Qian).

Peer review under responsibility of Chinese Pharmaceutical Association and Institute of Materia Medica, Chinese Academy of Medical Sciences.

https://doi.org/10.1016/j.apsb.2021.08.021

2211-3835 © 2022 Chinese Pharmaceutical Association and Institute of Materia Medica, Chinese Academy of Medical Sciences. Production and hosting by Elsevier B.V. This is an open access article under the CC BY-NC-ND license (http://creativecommons.org/licenses/by-nc-nd/4.0/).

© 2022 Chinese Pharmaceutical Association and Institute of Materia Medica, Chinese Academy of Medical Sciences. Production and hosting by Elsevier B.V. This is an open access article under the CC BY-NC-ND license (http://creativecommons.org/licenses/by-nc-nd/4.0/).

1. Introduction

Breast cancer is the leading cause of global cancer incidence in 2020, with an estimated 2.3 million new cases, representing 11.7% of all cancer cases. It is the first leading cause of female cancer mortality worldwide, with 680,000 deaths[1]. In clinic, chemotherapy is one of conventional treatment methods for breast cancer[2,3]. Nevertheless, most chemotherapeutic drugs have uncontrolled release behavior and weak targeting ability, which easily induce systemic toxicity[4,5]. To break through those barriers, nanomaterials have been investigated to deliver chemotherapeutic drugs into tumors, constructing newer nanomedicines. These nanomedicines are superior to conventional chemotherapeutic drugs, it can significantly reduce the systemic toxicity of chemotherapeutic drugs and improve the efficacy of chemotherapy[6−8]. However, due to the complex pathogenesis of tumors, the efficacy of mono-chemotherapy regimen is usually unsatisfactory, while multiple combination therapy holds promising prospects in cancer treatment[9−11]. Photothermal therapy (PTT) as a promising therapeutic model has emerged and attracted widespread interest owing to its minimal invasiveness and specific spatial and temporal selectivity[12−16]. Currently, with iron oxide nanoparticles (NanoTherm, Magforce) have obtained clinical approval for PTT in Europe, PTT is expected to have a revolutionary clinical impact. Therefore, numerous photothermal agents have been explored as options to obtain better therapeutic effect[17−20]. Accordingly, it is urgent to develop a combined chemo-photothermal therapy nanosystem that can synchronously deliver chemotherapeutic drug and photothermal agent to the tumor site for the synergistic treatment of breast cancer.

Camptothecin (CPT), a DNA topoisomerase I inhibitor, possesses strong antitumor activities, but its clinical application is hindered by its intrinsic high toxicity, poor water-solubility, and structural instability[21]. Great efforts have been made to resolve this issue to meet clinical needs[22−26]. For example, irinotecan and topotecan, as typical representatives of CPT derivatives, are widely used in the clinical treatment of cancer diseases, but they still lack of poor circulation and targeting ability *in vivo*[27,28]. In addition, a large number of physically loaded CPT nanoformulations have been constructed to achieve good systemic circulation and target tumor cells[29,30], but due to the simple physical encapsulation and instability of carrier *in vivo*, CPT easily leaked from carrier in systemic circulation, resulting in low therapeutic effect and severe side effects. To solve this issue, nano-sized CPT prodrug strategies have been adopted, many studies have polymerized blocks of reduction-responsive CPT prodrug monomers for self-assembly, resulting in a nano-prodrug with high CPT loading content and loading stability as well as controlled release of CPT under physiological conditions that are specific for tumor cells[31,32]. Among various reduction-responsive bonds, disulfide bonds are some of the most frequently used reduction-sensitive linkages that have been widely explored and could be readily cleaved by the glutathione (GSH) within tumor cells, which contains about a 100 to 1000 times higher concentration of GSH than the extracellular environment[33,34].

At present, prussian blue nanoparticles (PB NPs), a mixed-valence transition metal hexacyanoferrates with the general formula of $Fe_4[Fe(CN)_6]_3 \cdot nH_2O$[35−37], have been approved by the US Food and Drug Administration (FDA) for the treatment of radioactive exposure in the clinic for many years and can also serve as effective PTT nanocarriers due to their strong absorption in the near-infrared (NIR) region and ease of modification[38−40]. PB NPs have an advantage over some organic photothermal dyes, such as indocyanine green (ICG), new indocyanine green (IR820, IR780), which in general are easily photobleached[41−43]. Furthermore, compared with other inorganic photothermal agents, including gold nanostructures, carbon-based nanomaterials, and noble metal-based nanostructures, PB NPs are more biodegradable and have lower potential long-term toxicity[44−48]. Therefore, PB NPs have excellent photothermal effects and biodegradability, which are important factors to achieve the development of cancer PTT technology. In addition, PB NPs can also be used as a photoacoustic imaging (PAI) contrast agent to allow real-time tracking[49−52]. In recent years, many groups, including ours, have explored the applications of PB NPs-based nanoagents as photothermal agents for cancer treatment in animal models[16,53,54].

Here, we designed and synthesized a multifunctional nanoparticle system (PCRHNs) with PB NPs as the seed nanoparticles and conjugated with amphiphilic block copolymers (COOH-PEG_{4000}-$PssCPT_9$, which was composed of hydrophilic carboxyl-poly(ethylene glycol)$_{4000}$ (COOH-PEG_{4000}) and a polymerized block of reduction-responsive camptothecin prodrug monomer ($PssCPT_9$)) for chemo-photothermal therapy. Although synthetic nanoparticles have shown promising passive tumor targeting behavior through the enhanced permeability and retention (EPR) effect, this passive targeting effect is suboptimal[55]. Furthermore, the rapid clearance of synthetic nanoparticles by the mononuclear phagocyte system (MPS) during *in vivo* circulation leads to a low delivery efficiency of the nanoparticles to tumor sites[56−58]. To overcome that predicament, the tumor-targeting peptide cyclo(Asp-D-Phe-Lys-Arg-Gly) (cRGD) and hyaluronic acid (HA) were introduced into the nanosystem to construct PCRHNs. This is because cRGD has high binding affinity with the $\alpha_v\beta_3$ integrin that is overexpressed in many cancer cell lines, leading to high accumulation of cRGD-modified nanoparticles in tumor tissues[59]; HA, an anionic glycosaminoglycan that is widely existing in the human body, can be used to modify nanoparticles to obtain better biocompatible nanocarriers[60]. In addition, taking advantage of the strong NIR absorbance of PCRHNs, PAI test was carried out to provide the optimal time point for PTT *in vivo* to achieve highly effective tumor destruction. Meanwhile, in response to the GSH inside tumor cells, the active CPT drugs were released for chemotherapy. Therefore, PCRHNs combines chemotherapy with photothermal therapy has achieved significantly synergistic antitumor effects *in vitro* and *in vivo*, and no obvious signs of toxicity were observed for mice within the observation period of one month after injection with a high dose of PCRHNs (40.0 mg/kg).

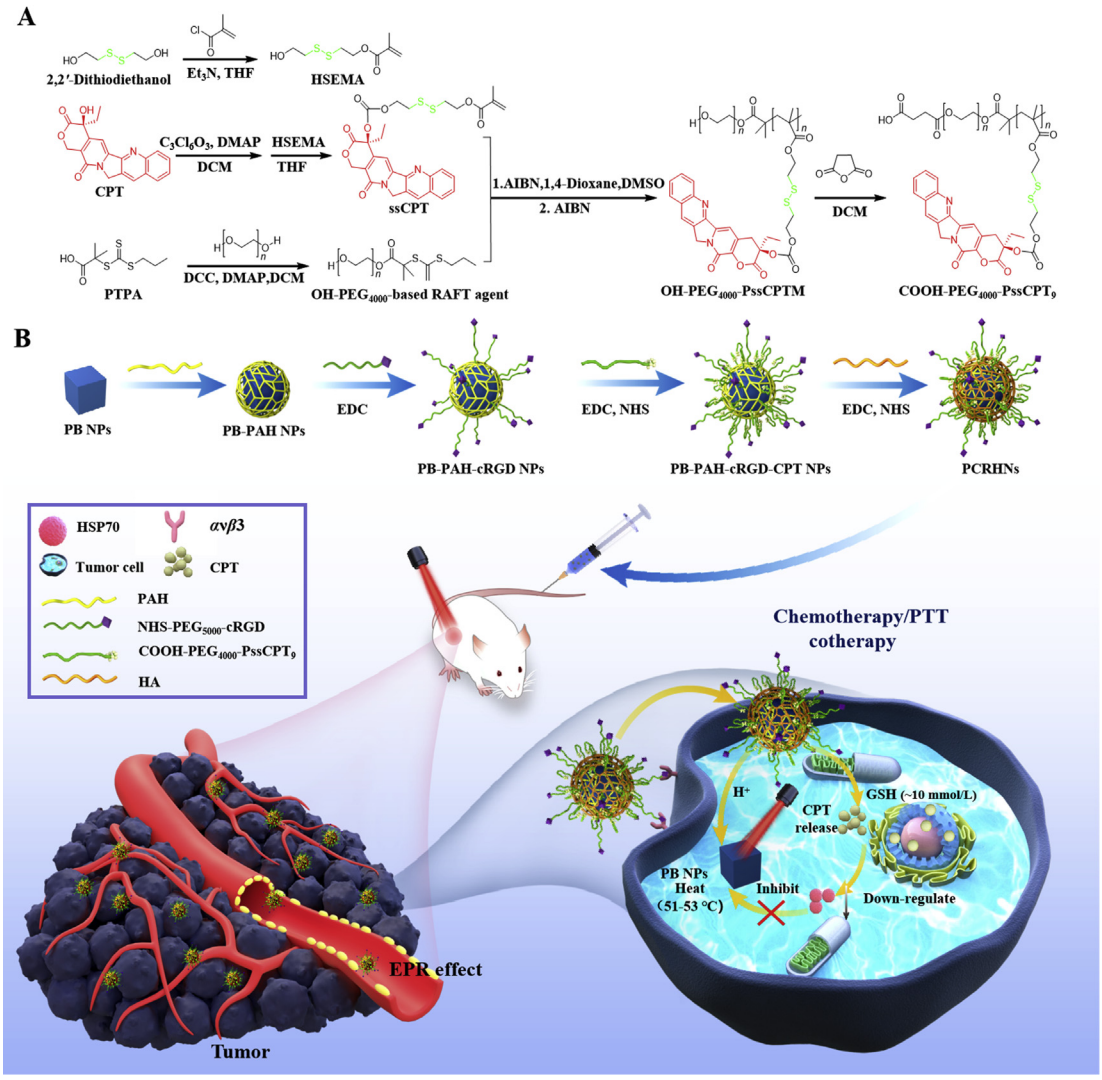

Scheme 1 Schematic presentation of the multifunctional nanoparticles PCRHNs for chemo-photothermal combinational therapy against breast cancer. (A) Synthesis scheme of amphiphilic block copolymers (COOH-PEG_{4000}-$PssCPT_9$). (B) Synthesis scheme of PCRHNs, and schematic illustration of PCRHNs for synergistic tumor chemotherapy/photothermal therapy.

Moreover, we found that the hyperthermia-induced upregulation of heat shock protein 70 (HSP70) in the tumor cells could be inhibited by CPT (Scheme 1B). HSP70 is molecular chaperone capable of repairing the heat-denatured proteins, and its expression increases rapidly upon exposure to hyperthermia, which results in enhanced tumor thermoresistance[61]. These results demonstrated that PCRHNs are promising therapeutic way for breast cancer targeted therapy.

2. Materials and methods

2.1. *Materials*

Polyethylene glycol (PEG, MW = 4.0 kDa) and GSH were purchased from Sigma−Aldrich. Succinimide ester-polyethylene $glycol_{5000}$-cyclo (Asp-D-Phe-Lys-Arg-Gly) (NHS-PEG_{5000}-cRGD) was purchased from Beijing Jenkem Technology Co., Ltd. CPT was purchased from Dalian Meilun Biology Technology Co., Ltd. Citric acid monohydrate, triphosgene, $K_4[Fe(CN)_6]\cdot 3H_2O$, $FeCl_3\cdot 6H_2O$, polyallylamine hydrochloride (PAH, MW = 15.0 kDa), and 2,2′-dithiodiethanol were purchased from Shanghai Aladdin Chemistry Co., Ltd. HA (MW = 32.0 kDa) was purchased from Bloomage Biology Technology Co., Ltd. HSP70 antibody was purchased from Abcam. Lyso-Tracker red and 2-(4-amidinophenyl)-6-indolecarbamidine dihydrochloride (DAPI) were purchased from Beyotime Biotechnology Co., Ltd. Calcein-AM/propidium iodide (Calcein-AM/PI) Double Stain Kit, fluorescein isothiocyanate (FITC), and Annexin V-FITC/PI Apoptosis Detection Kit were purchased from Shanghai Yeasen Biotechnology Co., Ltd. Murine 4T1 breast cancer cells were obtained from Chinese Academy of Sciences Cells Bank (Shanghai, China). All the materials used in this study were analytic grade and used without further purification.

2.2. *Synthesis of OH-PEG_{4000}-based RAFT agent*

The OH-PEG_{4000}-based reversible addition−fragmentation chain transfer (RAFT) agent was prepared according to similar procedures

reported previously[62–64]. Firstly, 2-propylsulfanylthiocarbonylsulfanyl-2-methylpropionic acid (PTPA) was synthesized according to An's method[62]. And then, PEG_{4000} (10.0 g, MW = 4.0 kDa), PTPA (0.59 g), and dry CH_2Cl_2 (100.0 mL) were charged into a 250 mL round-bottom flask and then cooled to 0 °C in an ice-water bath. A mixture containing *N*,*N*′-dicyclohexylcarbodiimide (DCC, 0.83 g, 4.0 mmol/L), 4-(dimethylamino) pyridin (DMAP, 49.0 mg, 0.4 mmol/L), and dry CH_2Cl_2 (25.0 mL) was added dropwise over 1 h. The reaction mixture was then stirred at room temperature for 48 h. After filtration and evaporating all the solvents, the residues were diluted with CH_2Cl_2 and then precipitated into an excess of cold diethyl ether. The above dissolution−precipitation cycle was repeated three times. After drying in a vacuum oven overnight, OH-PEG_{4000}-based RAFT agent was obtained as a slightly yellowish powder (9.1 g, yield, 91.0%).

2.3. Synthesis of COOH-PEG_{4000}-$PssCPT_9$ polyprodrug

The COOH-PEG_{4000}-$PssCPT_9$ was synthesized by RAFT polymerization method. Firstly, 2-((2-hydroxyethyl) disulfanyl) ethyl methacrylate (HSEMA) and reduction-responsive CPT monomer (ssCPT) were synthesized according to Hu's method[31]. Then, the OH-PEG_{4000}-PssCPTM was synthesized according to similar procedures reported previously[61]. Briefly, OH-PEG_{4000}-based RAFT agent (200.0 mg, 0.05 mmol/L), ssCPT (600.0 mg, 1.05 mmol/L), and 2,2′-azobis (2-methylpropionitrile) (AIBN, 0.33 mg, 0.002 mmol/L) were dissolved in 1,4-dioxane/dimethyl sulfoxide (6.0 mL, 1:1, *v*/*v*) and added into a flask. The flask was sealed under dry argon and the polymerization was carried out at 80 °C for 24 h. The product was further treated with an excess of AIBN (20 equiv.) in CH_2Cl_2 to remove terminal trithiocarbonate moieties. After stirring at 60 °C for 6 h, the solution was precipitated into an excess of diethyl ether, the residues were dissolved in CH_2Cl_2 and precipitated into diethyl ether, and the above dissolution−precipitation cycle was repeated for three times. The final product (OH-PEG_{4000}-PssCPTM) was dried in a vacuum oven overnight at room temperature, yielding a pale solid powder (654.9 mg, yield: 81.8%). Finally, OH-PEG_{4000}-PssCPTM (200.0 mg, 0.05 mmol/L), succinic anhydride (SA, 25.0 mg, 0.25 mmol/L) were dissolved in dry CH_2Cl_2 (25.0 mL) and charged into a 250 mL round-bottom flask. The flask was stirred at 45 °C for 24 h under dry nitrogen atmosphere. After that the solution was precipitated into an excess of diethyl ether, the residues were dissolved in CH_2Cl_2 and precipitated into diethyl ether, and the above dissolution−precipitation cycle was repeated for three times. The final product was dried in a vacuum oven overnight at room temperature, yielding a pale solid powder (192.6 mg, yield: 96.3%). The obtained polyprodrug were denoted as COOH-PEG_{4000}-$PssCPT_9$.

2.4. Preparation of PCRHNs

PB NPs were synthesized according to the method published previously[65]. In a typical procedure, $FeCl_3 \cdot 6H_2O$ (5.4 mg, 0.02 mmol/L) was dissolved in deionized water (20.0 mL) containing citric acid monohydrate (107.0 mg, 0.5 mmol/L) and stirred at 60 °C. A mixture containing $K_4[Fe(CN)_6] \cdot 3H_2O$ (8.4 mg, 0.02 mmol/L) and citric acid monohydrate (107.0 mg, 0.5 mmol/L) in deionized water (20.0 mL) was added dropwise. After centrifuging and washing with deionized water three times, the obtained PB NPs were dissolved in deionized water for future use.

PCRHNs were synthesized through the layer-by-layer method. First, 2.0 mL of PB NPs (2.0 mg/mL) was added dropwise into 2.0 mL PAH solution (5.0 mg/mL), and the mixture was stirred for 4 h; a PB-PAH solution was obtained and purified by filtration through 100 kDa molecular weight cut-off (MWCO) filters (Millipore) to remove excess PAH molecules. Second, the above PB-PAH solution was added dropwise into 2.0 mL NHS-PEG_{5000}-cRGD aqueous solution (1.0 mg/mL) and then stirred for 4 h; a PB-PAH-cRGD solution was obtained and purified by filtration through 100 kDa MWCO filters. Third, COOH-PEG_{4000}-$PssCPT_9$ (10.0 mg), *N*-(3-dimethylaminopropyl-*N*-ethylcarbodiimide) hydrochloride (EDC, 10.0 mg), and *N*-hydroxysuccinimide (NHS, 10.0 mg) were dispersed in 1.0 mL of DMSO and then stirred for 1 h before being added into the above PB-PAH-cRGD solution. The reaction continued for 12 h; a PB-PAH-cRGD-CPT solution was obtained and was purified by filtration through 100 kDa MWCO filters. Lastly, EDC and NHS (each for 10.0 mg) were added into 2.0 mL HA solution (3.0 mg/mL); the solution was stirred for 1 h and added into the PB-PAH-cRGD-CPT solution under ultrasonication. After adjusting the pH to 7.4, the reaction was stirred overnight, yielding a PCRHNs solution that was purified by filtration through 100 kDa MWCO filters several times and stored at 4 °C for future use.

To prepare the FITC-PCRHNs, 5.0 mg of PB-PAH-cRGD-CPT NPs was dispersed in 2.0 mL of deionized water, and then 1.0 mg of FITC was added into the mixture solution. The reaction continued for 24 h under stirring in the dark. Afterward, the PB-PAH-cRGD-CPT-FITC NPs was purified by filtration through 100 kDa MWCO filters with several times. Then, EDC and NHS (each for 10.0 mg) were added into 2.0 mL HA solution (3.0 mg/mL); the solution was stirred for 1 h and added to the PB-PAH-cRGD-CPT-FITC NPs solution under ultrasonication and then stirred for overnight. The FITC-PCRHNs solution was obtained and was purified by filtration through 100 kDa MWCO filters with several times, and stored at 4 °C for future use.

2.5. Characterization of PCRHNs

The particle size and zeta potential of the PCRHNs were measured by dynamic light scattering (DLS, Nano-ZS 90, Malvern Instruments, UK). The surface morphology of the PCRHNs was observed by scanning electron microscopy (SEM, JSM-7500F, JEOL, Japan). The micromorphology of PCRHNs was investigated by transmission electron microscopy (TEM, Tecnai G2 F20 S-TWIN). The crystallization of PCRHNs was evaluated by X-ray diffraction (XRD, EMPYREAN, PANalytical B.V., Netherlands). The optical absorption of PCRHNs was measured by UV−visible spectrometer (UV-2600, Shimadzu, Japan), all samples were diluted to a certain concentration before the measurement. The compositions of PCRHNs were measured by thermogravimetric analysis (TGA, TGA/DSC2 Mettler Toledo, Switzerland). Fourier transform infrared spectroscopy (FT-IR) spectra were acquired with a Nicolet-6700 spectrometer (Thermo Scientific, Waltham, MA, USA) using the KBr.

2.6. Photothermal performance of PCRHNs

The photothermal conversion of PCRHNs was evaluated by detecting the temperature variation of the PCRHNs solution (1.0 mL) under irradiation with an 808 nm laser (Hi-Tech Optoelectronics Co., Ltd., Beijing, China) at a power density of 1.0 W/cm^2 for 5 min. A certain amount of PCRHNs was dissolved in phosphate buffered saline (PBS, pH = 7.4) to prepare solutions with concentrations of 0.02, 0.05, 0.1, 0.2, and 0.5 mg/mL,

respectively. The temperature was detected by digital thermometer and fluke infrared thermal imaging system (Ti-32, Fluke). PBS was used as a negative control. To evaluate the stability of the photothermal conversion of PCRHNs, the on/off cycle irradiation experiment was carried out. The 0.5 mg/mL PCRHNs solution was prepared and irradiated by an 808 nm laser for 3 min and then turned off. After 3 min, the laser was turned on again. This process was repeated for five cycles, and the temperature variation was recorded. The variation of the UV−visible spectrum of PCRHNs before and after the irradiation were measured by UV−visible spectrometer.

2.7. *In vitro CPT release*

To evaluate the CPT release behaviors of the PCRHNs *in vitro*, three pH conditions were selected to simulate the normal physiological (pH 7.4), tumor tissues (pH 6.4), and endo/lysosome microenvironment (pH 5.0), respectively. PCRHNs (4.0 mg) were dispersed in 2.0 mL buffer of different pH solutions (containing 0 mmol/L GSH, 1.0 mmol/L GSH or 10.0 mmol/L GSH) and transferred to dialysis bags (molecular weight cutoff: 3500 Da) immersed in 20.0 mL of the same buffered media at 37 °C. Periodically, 2.0 mL of the medium was taken out and replaced with the same volume of fresh buffer solution. The amount of CPT was measured by high-performance liquid chromatography (HPLC) on a system equipped with an Altima C18 analytic column (250 mm × 4.6 mm, 5 μm) by the gradient elution of solvent A (CH_3CN containing 0.2% acetic acid) and solvent B (H_2O containing 0.2% acetic acid) at a flow rate of 1.0 mL/min at 35 °C, monitored at 368 nm by a diode array detector (DAD).

2.8. *Cellular uptake and hemolysis test*

To estimate the cellular uptake of 4T1 to PCRHNs, the 4T1 cells were seeded in a 6-well plate at 5×10^5 cells per well. After preincubation for 24 h, CPT, PB-PAH-CPT-HA NPs, and PCRHNs were added to the well to incubate with the cancer cells for different durations, in which the net concentration of the CPT substrate in all sample groups has been maintained at 20.0 μg/mL. After incubating for 30 min, 1, 2, 4, or 6 h, cells were washed with cold PBS more than three times. Then, the fluorescence images of the cancer cells were taken by confocal laser scanning microscopy (CLSM, LSM 510 Meta NLO, Zeiss, Germany). A flow cytometry assay was used to quantitatively calculate the cellular uptake of 4T1 to PCRHNs. The 4T1 cells were seeded in a 6-well plate at 5×10^5 cells per well. After being preincubated for 24 h, FITC-PCRHNs (20.0 μg/mL CPT-equivalent dosage) was added to the well to incubate with the cancer cells for different durations. After incubating for 30 min, 1, 2, 4, or 6 h, cells were washed with cold PBS more than three times. Then, these treated cells were collected to determine the cellular uptake using the Beckman coulter flow cytometer (Navios, Beckman, USA).

The hemolytic study was performed *in vitro* according to our previous reports[53]. Briefly, 0.5 mL of the prepared PCRHNs (4.0, 2.0, 1.0, 0.5, 0.2 mg/mL) in saline was diluted to 2.5 mL using saline and added to 2.5 mL of rabbit erythrocyte suspension (2%) in saline at 37 °C. Distilled water and saline were employed as the positive and negative controls, respectively. After 3 h, the erythrocyte suspension was centrifuged, and the color of the supernatant was compared to that of the controls. Also, the absorption of the supernatant at 570 nm was measured by a UV−vis spectrophotometer, and the hemolysis ratio was calculated by comparing it to that of the positive control.

2.9. *In vitro cytotoxicity assay*

For the *in vitro* cytotoxicity assay, 4T1 cells were seeded at 1×10^4 cells per well in a 96-well plate. After preincubation for 24 h, the original culture medium was removed, and fresh culture medium was added with varying concentrations of free CPT, PB NPs, PB NPs/CPT (8:1, *m*/*m*), PB-PAH-CPT-HA NPs, and PCRHNs. Four hours later, the culture medium of each sample was replaced with fresh culture medium with penicillin-streptomycin after rinsing once with PBS buffer, and the cells were cultured for another 24 h. To the groups treated with an NIR laser (808 nm, 1.0 W/cm^2), after the addition of fresh culture medium, the NIR laser was introduced, and the cells were irradiated for 5 min before another 24 h of culturing. Finally, cell viability was determined by performing a methyl thiazolyl tetrazolium (MTT) assay. Untreated cells in the medium were used as controls. All experiments were carried out in quadruplicate.

To visualize the chemotherapy/PTT cotherapy of cancer cells *in vitro*, live/dead costaining was performed. 4T1 cells were seeded into a 6-well plate and preincubated for 24 h. After the cell confluence reached about 80%, the cells were treated with different conditions (i: saline; ii: saline + laser; iii: CPT (20.0 μg/mL); iv: PCRHNs (200.0 μg/mL); v: PB NPs + laser (160.0 μg/mL); vi: PB NPs/CPT + laser (180.0 μg/mL, 8:1, *m*/*m*); vii: PB-PAH-CPT-HA NPs + laser (200.0 μg/mL); and viii: PCRHNs + laser (200.0 μg/mL)). Four hours later, the culture medium of each sample was replaced with fresh culture medium with penicillin-streptomycin after rinsing once with PBS buffer, and the cells were cultured for another 24 h. To the groups treated with an NIR laser (808 nm, 1.0 W/cm^2), after the addition of fresh culture medium, the NIR laser was introduced and the cells were irradiated for 5 min before another 24 h of culturing. Then, these treated cells were stained with Calcein-AM/PI and analyzed by CLSM. To determine the cell apoptosis ratio (%) after treatment with the PCRHNs system, the cells were cultured for another 6 h after being replaced with fresh culture medium, and stained with the Annexin V-FITC/PI cell assay kit following the instructions. Finally, the Beckman coulter flow cytometer was applied to determine the cell apoptosis in each group.

2.10. *Western blotting assays for HSP70 expression characterization*

The expression levels of HSP70 were identified by Western blotting assays. In brief, 4T1 cells were seeded in 6-well plates at a density of 5×10^5 cells per well for 24 h. Then the cells were treated with different conditions (a: saline; b: saline + laser; c: PB NPs (160.0 μg/mL); d: CPT (20.0 μg/mL); e: PCRHNs (200.0 μg/mL); f: PB NPs + laser (160.0 μg/mL); g: PB NPs/CPT + laser (180.0 μg/mL, 8:1, *m*/*m*); h: PCRHNs + laser (200.0 μg/mL); a′: saline under incubation at 40 °C; b′: saline + laser under incubation at 40 °C; c′: PB NPs (160.0 μg/mL) under incubation at 40 °C; d′: CPT (20.0 μg/mL) under incubation at 40 °C; e′: PCRHNs (200.0 μg/mL) under incubation at 40 °C; f′: PB NPs + laser (160.0 μg/mL) under incubation at 40 °C; g′: PB NPs/CPT + laser (180.0 μg/mL, 8:1, *m*/*m*) under incubation at 40 °C; h′: PCRHNs + laser (200.0 μg/mL) under incubation at 40 °C), in which the net concentration of the CPT substrate in all sample groups has been maintained at 20.0 μg/mL. Six hours later, the culture medium of each sample was replaced with fresh culture medium with penicillin-streptomycin after rinsing once with PBS buffer, and the cells were cultured for another 12 h. To the groups treated with an NIR laser (808 nm, 1.0 W/cm^2), after the addition of fresh culture

medium, the NIR laser was introduced, and the cells were irradiated for 5 min before another 12 h of culturing. Afterward, Western blot analyses were performed according to the protocols for the routine with antibodies against HSP70, and actin was employed as a protein loading control. Finally, cell viability was determined by MTT assay.

2.11. Tumor model

Female BALB/c mice (5−6 weeks old) were all purchased from Beijing Vital River Laboratory Animal Technology Co., Ltd. All animal experiments were performed under the supervision of the animal guidance of Stake Key Laboratory of Biotherapy, West China Hospital, Sichuan University. 4T1 subcutaneous tumors were generated by subcutaneous injection of 1×10^6 cells in ~100 μL serum-free RMPI-1640 medium onto the back of each female BALB/c mouse.

2.12. In vivo blood circulation experiments and time-dependent biodistribution

The *in vivo* pharmacokinetic tests of PCRHNs, PB-PAH-CPT-HA NPs and CPT were carried out on the SD female rats (~250 g, each group comprised three rats). Briefly, PCRHNs, PB-PAH-CPT-HA NPs, or CPT (2.0 mg/kg CPT-equivalent dosage) were intravenously injected into each rat of different groups through the tail vein. At predetermined time points, orbital vein bleeds (~0.4 mL) were collected into tubes containing heparin and then incubated at 4 °C. All of the blood samples were centrifuged to obtain plasma; 50.0 μL plasma was added to 9 times the volume of methanol, and another 50.0 μL plasma was added to 9 times the volume of methanol containing 10.0 mmol/L of GSH. The mixtures were vortexed and kept at room temperature for 24 h; 10-hydroxycamptothecin was used as an internal standard. Finally, the plasma samples were measured by HPLC.

For the analysis of the *in vivo* time-dependent biodistribution of PCRHNs, PB-PAH-CPT-HA NPs, and CPT, the 4T1 cancer model was established in female BALB/c mice, when the tumor volumes reached about 400 mm^3, the tumor-bearing mice were randomly assigned to each group (each group comprised three mice). Briefly, PCRHNs, PB-PAH-CPT-HA NPs, or CPT (2.0 mg/kg CPT-equivalent dosage) were intravenously injected into each mice of different groups through the tail vein. At predetermined time points, the mice were sacrificed by cervical dislocation. The primary organs (heart, liver, spleen, lungs, kidneys) and tumor were removed and washed with precooled normal saline. Then the tissue samples were weighed and stored at −20 °C until analysis by HPLC. Briefly, a certain amount of tissue sample was homogenized with 1.0 mL saline, using a tissue homogenizer (Ultra-Turrax T10 basic, IKA, Germany) for 5 min. Excess GSH was added to 500 μL tissue homogenate, which was vortexed at room temperature for 24 h; 10-hydroxycamptothecin was added as an internal standard and then extracted with a mixture of dichloromethane and methanol (10:1, *v*/*v*). Another 500 μL tissue homogenate was extracted directly without GSH treatment. The organic fraction was collected and dried under nitrogen gas. The residue was then dissolved with methanol, and the supernatant was injected into the HPLC system.

2.13. Photoacoustic imaging and photothermal conversion in vivo

The 4T1 cancer model was established in female BALB/c mice before PAI and photothermal conversion evaluation. In this experiment, when the tumor volumes reached about 400 mm^3, the tumor-bearing mice were randomly assigned to each group (each group comprised three mice). Briefly, 4T1 tumor-bearing mice were intravenously injected with PCRHNs (20.0 mg/kg) prior to imaging. For control groups, mice were treated with equal-weight PB-PAH-CPT-HA NPs or the same volume of saline. During our experiments, anesthesia was maintained using pentobarbital (50.0 mg/kg). PAI imaging was performed with a multispectral optoacoustic tomography scanner (MSOT, MSOT in Vision 128, iThera Medical GmbH, Germany) small animal scanner. The laser frequency was 10 Hz, with six wavelengths: 700, 715, 730, 760, 800, and 850 nm. The step length was 0.3 mm, and the speed of sound was −36. The temperature of the sink was 35 °C. Model-linear and linear regression were chosen as the reconstruction method and the multi-scale patch-based matrix regression (MSP) method, respectively. The MSP background wavelength was 715 nm.

The optimum time point for photothermal conversion of PCRHNs *in vivo* was performed in accordance the result of PAI. After 6 h of intravenous injection, the tumors were irradiated with an 808 nm laser at a power density of 1.5 W/cm^2 for 5 min. The tumor surface temperatures were recorded by a Fluke infrared thermal imaging system.

2.14. In vivo chemo-photothermal therapy

In this experiment, when the tumor volumes reached about 150 mm^3, the tumor-bearing mice were randomly divided into 16 groups (I: saline group; II: saline + laser group; III: CPT group (2.0 mg/kg); IV: PCRHNs group (20.0 mg/kg); V: PB NPs + laser group (16.0 mg/kg); VI: PB NPs/CPT + laser group (18.0 mg/kg, 8:1, *m*/*m*); VII: PB-PAH-CPT-HA NPs + laser group (20.0 mg/kg); VIII: PCRHNs + laser group (10.0 mg/kg, low-dose); IX: P CRHNs + laser group (20.0 mg/kg, medium-dose); X: PCRHNs + laser group (30.0 mg/kg, high-dose); to investigate the influence of the 808 nm laser irradiation cycles (LICs) on the therapeutic effect, another six groups were set up (XI−XII: PCRHNs + laser group (10.0 mg/kg, low-dose, two LICs/three LICs); XIII−XIV: PCRHNs + laser group (20.0 mg/kg, medium-dose, two LICs/three LICs); XV−XVI: PCRHNs + laser group (30.0 mg/kg, high-dose, two LICs/three LICs); each group comprised 5 mice). A total of 200 μL the aforementioned drug was intravenously injected into each mouse of the different groups. For laser groups, after 6 h, the tumors were irradiated with an 808 nm laser at a power density of 1.5 W/cm^2 for 5 min. After 24 h of administration, mice in the two laser irradiation cycles groups and three laser irradiation cycles groups were given a second irradiation. Finally, mice in the three laser irradiation cycles groups were given a third irradiation after 48 h of administration. The temperature changes at the tumor sites were recorded by a fluke infrared thermal imaging system. The tumor volumes and body weights of the mice were measured every other day. The length and width of the tumors were measured with a digital caliper, and the corresponding tumor volumes were calculated using Eq. (1):

$$\text{Volume} = \text{Width}^2 \times \text{Length}/2 \quad (1)$$

After 20 days of therapy, the mice were sacrificed for toxicity evaluation. Major organs, including the liver, spleen, kidney, heart, and lung, were harvested, fixed in 10% formalin, processed into paraffin, and then sectioned; the sections were then stained with hematoxylin and eosin (H&E) and imaged under a digital microscope (Leica QWin). The relevant tumors were collected for

proliferation and apoptosis evaluation Ki-67 staining and TUNNEL staining. Moreover, the tumor HSP70 expression was investigated immunefluorescence staining. For the analysis of animal survival, groups I−VII and XIV were selected, and the whole observation time was 60 days. During the whole observation period, the survival time of each mouse was recorded for subsequent analysis.

2.15. *Toxicology evaluations*

After all of the treatments were finished, healthy female BALB/c mice were randomly divided into three groups (each group comprised 15 mice). The PB NPs/CPT (8:1, *m*/*m*) and PCRHNs were intravenously injected into each mouse of the different groups at a dose of 40.0 mg/kg. The control group was injected with the same volume of saline. At various time points, five mice from each group were taken for orbital blood collection for a blood biochemistry assay and complete blood panel test. The blood was taken on Days 1, 7, and 30 after injection of nanomedicines. The serum biochemistry and complete blood panel were measured by Chengdu LiLai Biotechnology Co., Ltd. Major organs from the mice, including the liver, spleen, kidney, heart, and lung, were harvested, fixed in 10% formalin, processed into paraffin, and then sectioned; the sections were then stained with H&E and imaged under a digital microscope (Leica QWin).

2.16. *Statistics*

A statistical analysis was performed using OriginPro software (version 8.0). Data were represented as mean ± SD from at least three independent experiments. The differences among groups were calculated using ANOVA, and the results of $P < 0.05$ were considered as statistically significant. $^{*}P < 0.05$, $^{**}P < 0.01$, and $^{***}P < 0.005$ *vs*. saline or the relevant group are illustrated in figure legends.

3. Results and discussion

3.1. *Synthesis of COOH-PEG$_{4000}$-PssCPT$_9$ polyprodrug*

CPT is a well-known plant-derived complex antitumor monoterpenoid indole alkaloid with poor solubility in aqueous media. Here we describe the synthesis of relevant biological functions of amphiphilic block copolymers, COOH-PEG$_{4000}$-PssCPT$_9$, consisting of hydrophilic carboxyl-PEG$_{4000}$ (COOH-PEG$_{4000}$) and a polymerized block of reduction-responsive CPT prodrug monomer (PssCPT$_9$). The synthetic route to COOH-PEG$_{4000}$-PssCPT$_9$ is illustrated in Scheme 1A. First, the ssCPT was synthesized, and its chemical structure was confirmed by NMR and HRESIMS analysis (Supporting Information Fig. S1). Then, we employed the RAFT technique to polymerize the ssCPT using an OH-PEG$_{4000}$-based RAFT agent that was synthesized according to literature procedures[62−64]. The structure of the OH-PEG$_{4000}$-based RAFT agent was synthesized and confirmed by ^{1}H NMR (Fig. S2B). Finally, a polyprodrug amphiphile (OH-PEG$_{4000}$-PssCPTM) with CPT moieties in the hydrophobic block was synthesized (Supporting Information Fig. S3), and carboxyl groups with high activity were introduced into the amphiphilic polyprodrug to obtain the more malleable COOH-PEG$_{4000}$-PssCPTM. The average degree of polymerization (DP) for the PssCPTM block of the COOH-PEG$_{4000}$-PssCPTM was determined to be 9 by ^{1}H NMR (Supporting Information Fig. S4). The average molecular weight (MN) and molecular weight distribution (MW/MN) of COOH-PEG$_{4000}$-PssCPTM were determined by a gel permeation chromatography (GPC), revealing an MN of 9.9 kDa and MW/MN of 1.21 (Supporting Information Fig. S5 and Table S1), indicating that COOH-PEG$_{4000}$-PssCPTM with narrow molecular weight distributions. The CPT content of COOH-PEG$_{4000}$-PssCPTM was determined to be 42.5% according to a standard curve (Supporting Information Fig. S6a), which was consistent with the ^{1}H NMR result. The obtained polyprodrug amphiphile was denoted as COOH-PEG$_{4000}$-PssCPT$_9$.

3.2. *Preparation and characterization of PCRHNs*

To obtain a multifunctional nanoparticle system for breast cancer chemo-photothermal combinational therapy, PCRHNs was designed and constructed. The preparation process of PCRHNs is illustrated in Scheme 1B. As the first step for the synthesis of PCRHNs, PB NPs were synthesized by simply mixing aqueous solutions of $FeCl_3 \cdot 6H_2O$ and $K_4[Fe(CN)_6] \cdot 3H_2O$ in the presence of citric acid, which acted as the surface capping agent to ensure good colloidal stability in the formation of nanoparticles[65]. As shown by the TEM and SEM in Fig. 1A-1 and A-2, the as-prepared PB NPs had an average diameter of 83.8 nm, which was consistent with the result of the DLS (Fig. 1C).

To optimize the release profile of CPT *in vivo*, PB NPs were subsequently modified with NHS-PEG$_{5000}$-cRGD and HA. In brief, negatively charged PB NPs were modified by excess cationic polymer PAH electrostatic bindings, and the resultant intermediates were denoted as PB-PAH NPs. The zeta potentials of nanoparticles changed from −24.1 to 44.3 mV for PB NPs due to the amine groups in PAH when the free PB NPs were coated with the PAH. Afterward, a tumor-targeting polymer (NHS-PEG$_{5000}$-cRGD) and polyprodrug amphiphile (COOH-PEG$_{4000}$-PssCPT$_9$) were successively conjugated to PB-PAH NPs *via* amide formation. In this process, the series of feeding ratios of these two compounds was screened to obtain the optimal nanoparticles, and the results showed that the ratio of NHS-PEG$_{5000}$-cRGD to COOH-PEG$_{4000}$-PssCPT$_9$ was 1:5 (Supporting Information Table S2), which was as planned. The resultant intermediates were denoted as PB-PAH-cRGD NPs and PB-PAH-cRGD-CPT NPs, and their zeta potential decreased to 34.4 and 22.8 mV, respectively. Still, cationic nanoparticles tend to cause cytotoxicity and immune responses that may hamper their clinical translation[66,67]. HA, as an anionic biodegradable polymer, was introduced into the PB-PAH-cRGD-CPT NPs; after the coating of HA (MN = 32.0 kDa), the zeta potential decreased slightly to −8.8 mV. These results indicate the successful polymer adsorption on PB NPs (Fig. 1D), and the final nanoparticles were denoted as PCRHNs. Consistently, as the number of polymer layers increased during the assembly process, the sizes of PB NPs measured by DLS also increased. According to the DLS results (Fig. 1C and D), the average hydrodynamic diameter of PCRHNs were around 151.4 nm, while that of PB NPs was only about 83.8 nm, which suggested the successful surface modification of polymers on PB NPs. The morphology of resulting PCRHNs were characterized by TEM and SEM (Fig. 1B-1 and B-2), both of which indicated that PCRHNs were prepared successfully. Furthermore, the results of XRD (Supporting Information Fig. S7) revealed the PCRHNs retained the crystalline feature of the PB NPs.

The modification process was also monitored stepwise by FT-IR and TGA tests (Supporting Information Figs. S8 and S9). The

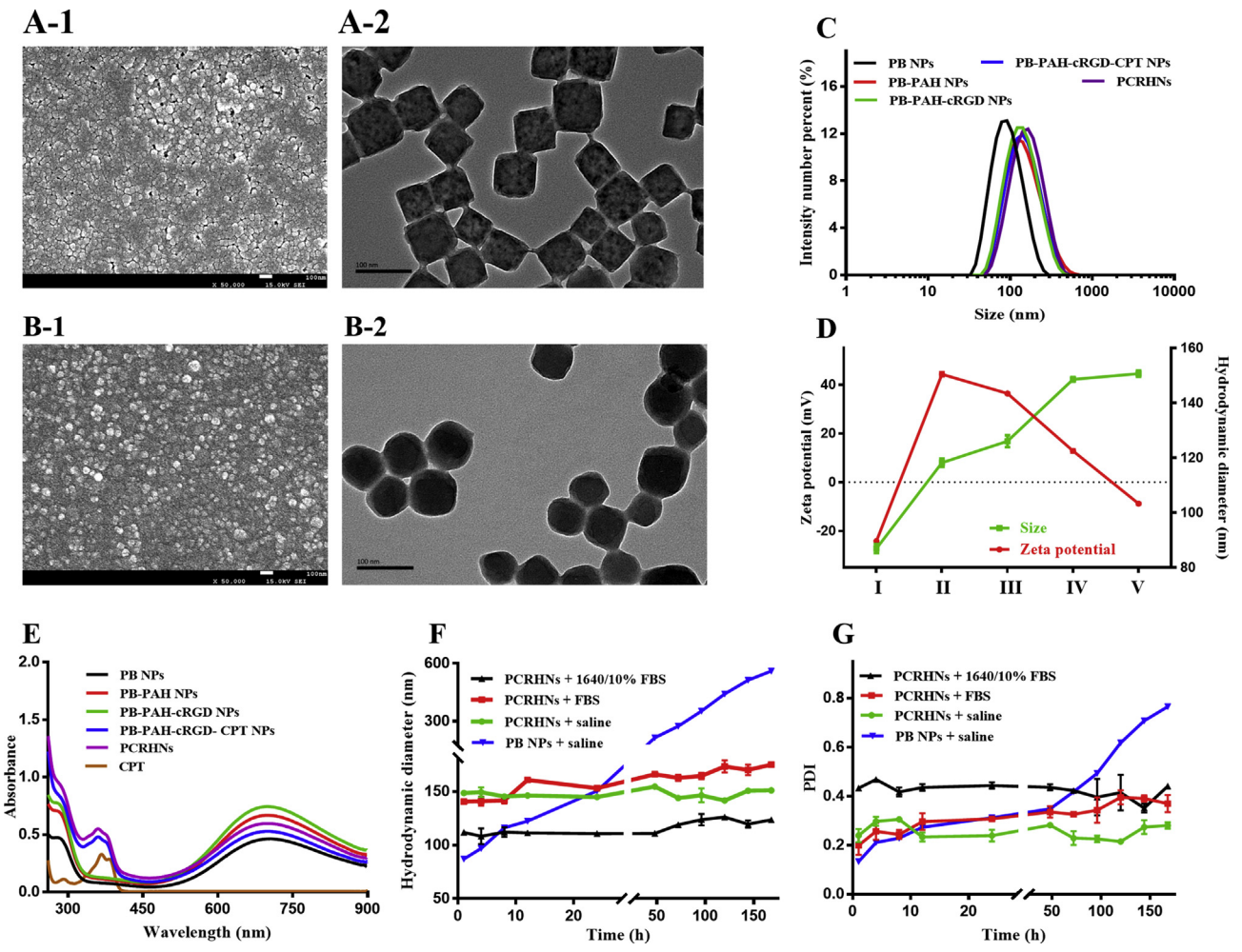

Figure 1 Characterization of PCRHNs. Representative SEM and TEM images of PB NPs (A-1) and (A-2), and PCRHNs (B-1) and (B-2), scale bar = 100 nm. DLS measured sizes (C) and zeta potentials (D) of nanoparticles after each step of surface coating (I: PB NPs; II: PB-PAH NPs; III: PB-PAH-cRGD NPs; IV: PB-PAH-cRGD-CPT NPs; V: PCRHNs). (E) UV−visible spectrum of nanoparticles after each step of surface coating in deionized water. DLS measured size (F) and PDI (G) changes of PB NPs and PCRHNs incubated in different conditions. Data were represented as mean ± standard deviation, $n = 3$.

FI-IR results of PB NPs showed a characteristic absorption peak at 2068 and 500 cm^{-1}, which was attributed to the −C≡N− bond and the bending mode of the Fe−C≡N−Fe. After surface modification with PAH, a new peak at 1525 cm^{-1} was appeared, which was ascribed to the $-NH_2$ groups. After conjugation with NHS-PEG_{5000}-cRGD, two characteristic peaks at 1109 and 1645 cm^{-1} were detected, which were assigned to the stretching vibration of $-CH_2-O-$ and −CO−NH−, respectively. Furthermore, after conjugation of COOH-PEG_{4000}-$PssCPT_9$, a characteristic peak at 1742 cm^{-1} was detected, which was assigned to the stretching vibration of −CO−O− in CPT. Finally, after conjugation of HA, a characteristic peak at 1026 cm^{-1} was detected, which was assigned to the stretching vibration of $-CH_2-O-$ in HA. TGA tests were also carried out, which revealed the chemical composition (*w*/*w*) of the products in each step. According to Supporting Information Fig. S9, PCRHNs comprised 3.1% PAH, 3.8% NHS-PEG_{5000}-cRGD, 17.7% COOH-PEG_{4000}-$PssCPT_9$, and 1.6% HA.

The optical absorption of PCRHNs were measured by a UV−visible spectrometer (Fig. 1E). Both PB NPs and PCRHNs displayed a broad absorption band from 500 to 900 nm with a strong absorption peak at ~720 nm. This demonstrates that PCRHNs may maintain the NIR absorption of PB NPs, which can be used as PTT nanocarriers. In addition, PB NPs has low absorption in the range of 300−550 nm, which favors the identification of the concentration of CPT after being loaded by PCRHNs. After the loading of CPT, a characteristic peak of CPT at 368 nm could be found in the UV−visible spectrum of PCRHNs. This indicated that CPT was successfully loaded into PCRHNs. By calculation, the loading capacity of PCRHNs to CPT was 9.2 ± 0.3% according to a standard curve (Supporting Information Fig. S6B), which was consistent with the TGA results. Furthermore, the PCRHNs exhibited remarkably improved stability compared with PB NPs, without showing any sign of aggregation even after several days of incubation in various physiological solutions, including saline, cell medium, and serum (Fig. 1F and G), and the polydispersity index (PDI) value only changed minimally, which demonstrated the good stability of PCRHNs in a physiological environment.

3.3. *Photothermal conversion of PCRHNs*

To investigate the photothermal properties of PCRHNs, a series of PCRHNs solutions with different concentrations of 0.02, 0.05, 0.1,

0.2, and 0.5 mg/mL were irradiated by an NIR laser (808 nm, 1.0 W/cm^2) and measured by infrared (IR) thermal camera (Fig. 2A). According to the temperature curves (Fig. 2B), it was found that the temperature increase rate was dependent on the concentration of PCRHNs, and the temperature eventually increased by 33.4 °C after 5 min of irradiation when the concentration was 0.5 mg/mL, while the temperature of the PBS group only increased minimally (nearly 4 °C). In addition, as shown in Fig. 2C, it was observed that the photothermal conversion efficiency of PCRHNs remained at a high level even after five cycles of NIR laser irradiation (808 nm, 1.0 W/cm^2, each cycle lasted 3 min), and the absorption band of the PCRHNs solution showed no apparent change even after irradiation for 30 min (Fig. 2D). Fig. 2E and F shows that the photothermal conversion efficacy (η) of PCRHNs calculated was approximately 41.75%. The high NIR absorbance coefficient, strong photothermal performance, and excellent photothermal stability of PCRHNs make it an encouraging nanoagent for PTT cancer treatment.

3.4. *Reduction-responsive CPT release*

The CPT release from PCRHNs were studied under various conditions to verify the sensitivity of the nanoparticles to reductive conditions. In this work, considering to the *in vivo* fate of nanoparticles, three pH conditions were selected to simulate the normal physiological environment (pH 7.4), tumor tissues (pH 6.4), and endo/lysosome microenvironment (pH 5.0). We studied in detail the controlled drug release behavior of PCRHNs by using dialysis methods under different pH values and GSH concentrations. The amounts of released parent CPT drugs were quantified by using HPLC. As shown in Fig. 3A, less than 5% CPT release was observed for PCRHNs at a physiologic pH of 7.4 after 60 h in the absence of GSH, suggesting the excellent CPT retention capability of PCRHNs; However, the CPT was released relatively rapidly in the presence of GSH (1.0 or 10.0 mmol/L), reaching 32% or 77% after 60 h, respectively. The above observations indicated the release of CPT due to the GSH-induced cascade elimination reaction (Fig. 3D). However, for different pH values, the CPT release rate at pH 5.0 was higher than that of pH 7.4 and pH 6.4, while the release rate at pH 6.4 was slightly higher than that of pH 7.4, but lower than that of pH 5.0 (Fig. 3B and C). This was likely due to the protonation of imidazole moieties and increased interactions between GSH and PCRHNs. After incubating with GSH for 60 h, the residual CPT content of PCRHNs in each group was also measured by a UV−visible spectrometer, which confirmed that a large amount of CPT had been released from PCRHNs, and the UV−visible spectrum results were consistent with the HPLC results (Fig. 3E). These results revealed that PCRHNs could maintain high stability under bloodstream and normal physiological environments, while they released CPT drugs in cancer cells with a high content of GSH and low pH value, thus improving the anticancer effects.

3.5. *Cellular uptake and cytotoxicity*

Before PCRHNs were used for therapeutic application, we first examined the cellular uptake of PCRHNs against 4T1 cells (murine breast cancer cells). The cRGD peptide can bind to $\alpha_v\beta_3$

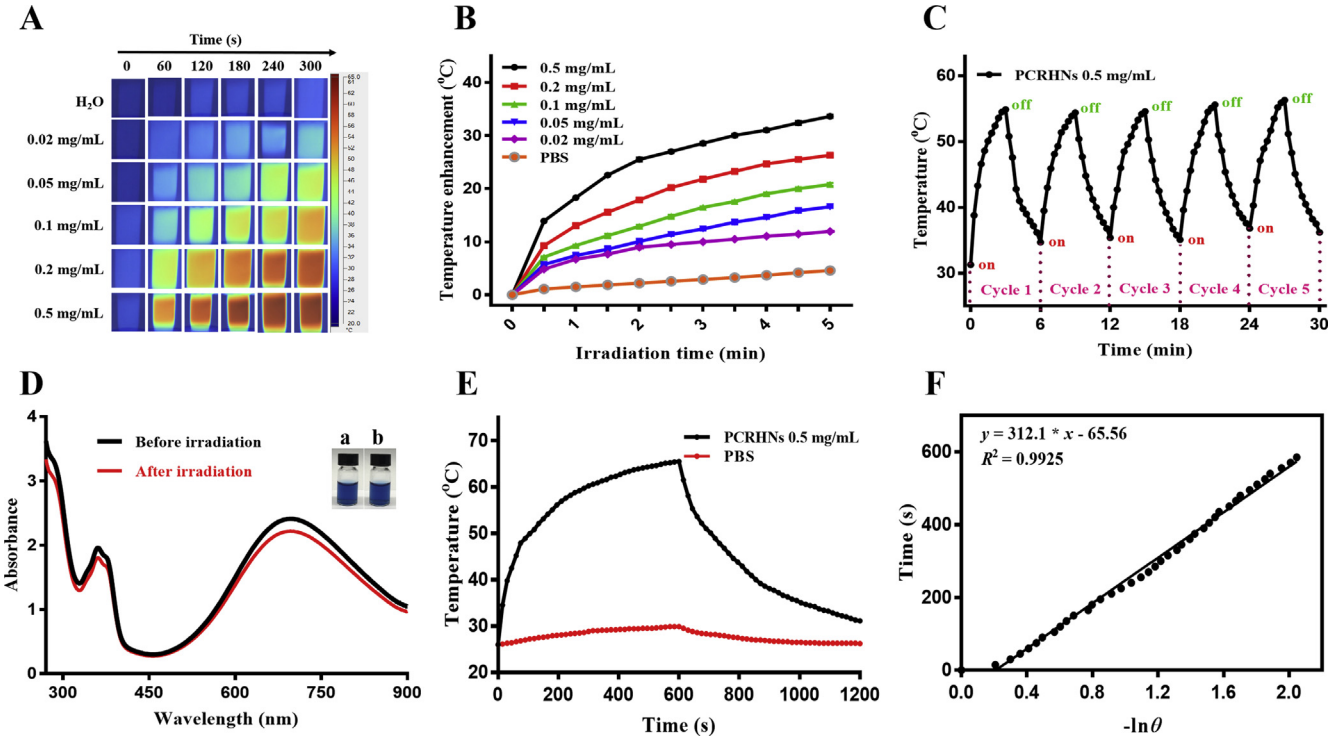

Figure 2 Photothermal performance of PCRHNs. Infrared thermal images (A) and photothermal heating curves (B) of PCRHNs with different concentrations (0.02, 0.05, 0.1, 0.2, 0.5 mg/mL) under 808 nm laser irradiation at the power density of 1.0 W/cm^2 for 5 min. (C) Temperature variations of PCRHNs solution (0.5 mg/mL) under irradiation with an 808 nm laser at the power density of 1.0 W/cm^2 for 5 cycles (3 min of irradiation for each cycle). (D) UV−visible spectrum of PCRHNs solution (0.5 mg/mL) before and after irradiation with an 808 nm laser at the power density of 1.0 W/cm^2 for 30 min. Inset: photos of PCRHNs solutions before (a) and after (b) laser irradiation. (E) and (F) Photothermal conversion efficiency of PCRHNs. Data were represented as mean ± standard deviation, $n = 3$.

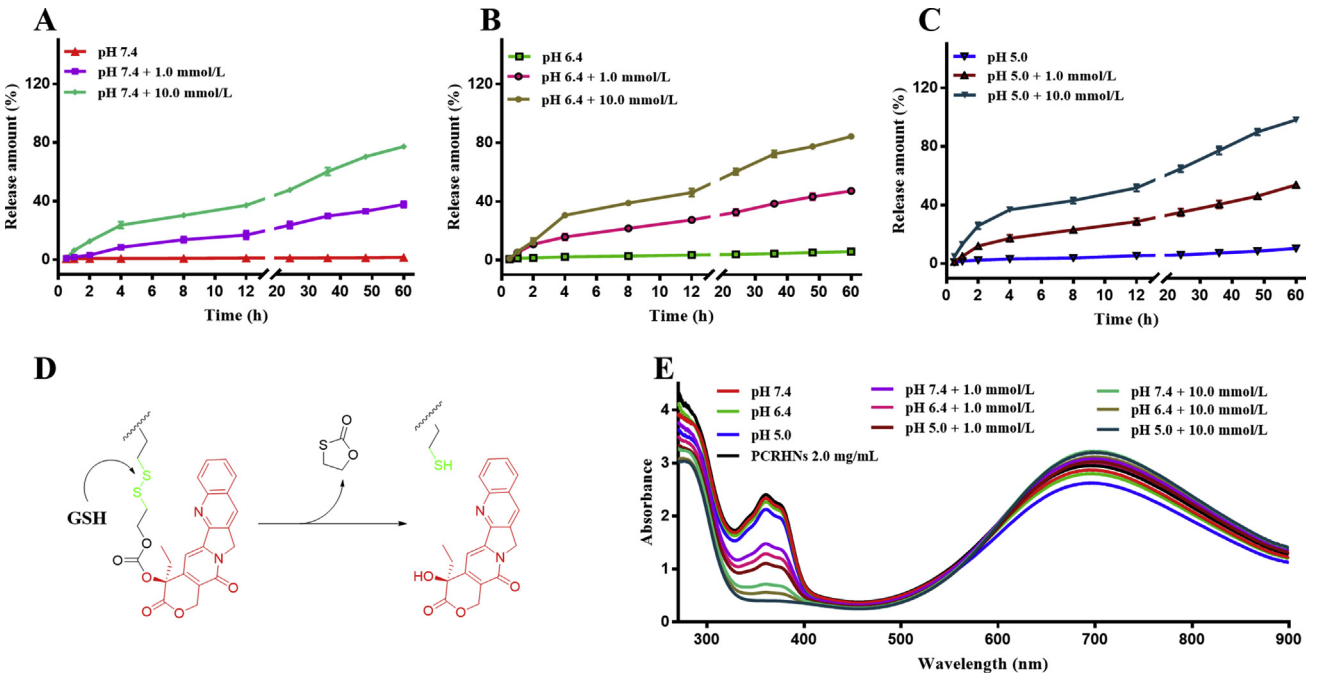

Figure 3 *In vitro* CPT release profiles of PCRHNs in pH = 7.4 (A), pH = 6.4 (B), pH = 5.0 (C) with different GSH concentrations (0, 1.0, 10.0 mmol/L). (D) Proposed mechanism of reduction-responsive CPT parent drug release from COOH-PEG$_{4000}$-PssCPT$_9$ polyprodrug amphiphiles. (E) UV−visible spectrum of PCRHNs solution before and after 60 h of incubation under different pH and GSH conditions. Data were represented as mean ± standard deviation, n = 3.

integrin, which is overexpressed on 4T1 cells[68,69]. Therefore, the exposure of cRGD peptides to PCRHNs is expected to achieve enhanced cellular internalization of PCRHNs. To demonstrate this, 4T1 cells treated with PCRHNs were analyzed using CLSM and flow cytometry during the time course from 30 min to 6 h incubation (Fig. 4). Much higher fluorescence intensity from CPT moieties was found in cells incubated with PCRHNs than in those incubated with free CPT and PB-PAH-CPT-HA NPs, demonstrating that the cellular internalization of PCRHNs was remarkably enhanced. The active cellular uptake rates were further confirmed by evaluating FITC labeled PCRHNs (FITC-PCRHNs) using flow cytometry. As shown in Fig. 4C, the cellular uptake of PCRHNs was very quick, reaching 95% within 30 min.

We further investigated the *in vitro* anticancer activities of PCRHNs by using an MTT assay. The MTT assay was used to determine the relative viabilities of 4T1 cells under exposure to PCRHNs (Fig. 5A). After cells were incubated with PB NPs at various concentrations for 24 h, no significant cytotoxicity of PB NPs was observed even at high concentrations up to 200.0 μg/mL. However, both free CPT and PCRHNs showed dose-dependent anticancer activities. Next, we used PCRHNs as the photothermal agent for *in vitro* cancer cell ablation under NIR laser irradiation (808 nm, 1.0 W/cm^2, 5 min). PCRHNs at various concentrations were incubated with 4T1 cells for 4 h and then irradiated by the NIR laser. An MTT assay was performed to quantitatively measure the relative cell viabilities after PTT treatment. PCRHNs + laser showed efficient anticancer activities, with an IC_{50} value of 20.1 μg/mL, which was 1.7 and 8.1 times lower than that of CPT and PB NPs + laser, respectively. Meanwhile, the anticancer activities of PCRHNs + laser were better than those of PB NPs/CPT + laser and PB-PAH-CPT-HA NPs + laser at the same dose. The superior antitumor efficacy is attributed to the higher cellular internalization of the PCRHNs and chemotherapy/PTT cotherapy. Furthermore, the cell killing effect after different treatments was investigated with live/dead cell fluorescence staining and flow cytometry (Fig. 5B and Supporting Information Fig. S10), and the results were in accordance with the MTT results. Meanwhile, the hemolytic study was performed on the prepared PCRHNs, and the result indicated that PCRHNs did not induce hemolysis or coagulation *in vitro*, as shown in Supporting Information Fig. S11.

3.6. *PCRHNs induced HSP70 suppression in vitro*

Based on these preliminary results, we speculated that there is a correlation between CPT-mediated chemotherapy and PB NPs-mediated PTT that leads to the synergistic therapeutic effect of PCRHNs. It is well known that hyperthermia increases heat shock proteins (HSPs) expression to enhance tumor thermoresistance[16]. CPT is a topoisomerase I (Top I) poison that causes DNA damage and regulates the expression of many proteins, including down-regulating HSPs expression in tumor cells[70−74]. Therefore, we speculate whether CPT can down-regulate HSPs to inhibit tumor thermoresistance, so that PCRHNs can exert superior antitumor efficacy. HSP70, a highly conserved and inducible heat shock protein, is an important family of HSPs with extensive and important physiological and pathological functions[75]. Hence, the expression level of HSP70 in 4T1 cells with different treatments was detected by Western blotting to evaluate the impact of chemotherapy and PTT on the expression of HSPs (Fig. 5C). After incubation at 40 °C (a′) or treatment with PB NPs + laser (f), the HSP70 level has increased to 1.65 and 1.32 times (Fig. 5D), respectively, compared with the saline group (a), which confirmed that the increase of ambient temperature can stimulate the expression of HSP70. In the saline + laser (b) and PB NPs (c) groups, the relative HSP70 level showed no significant change

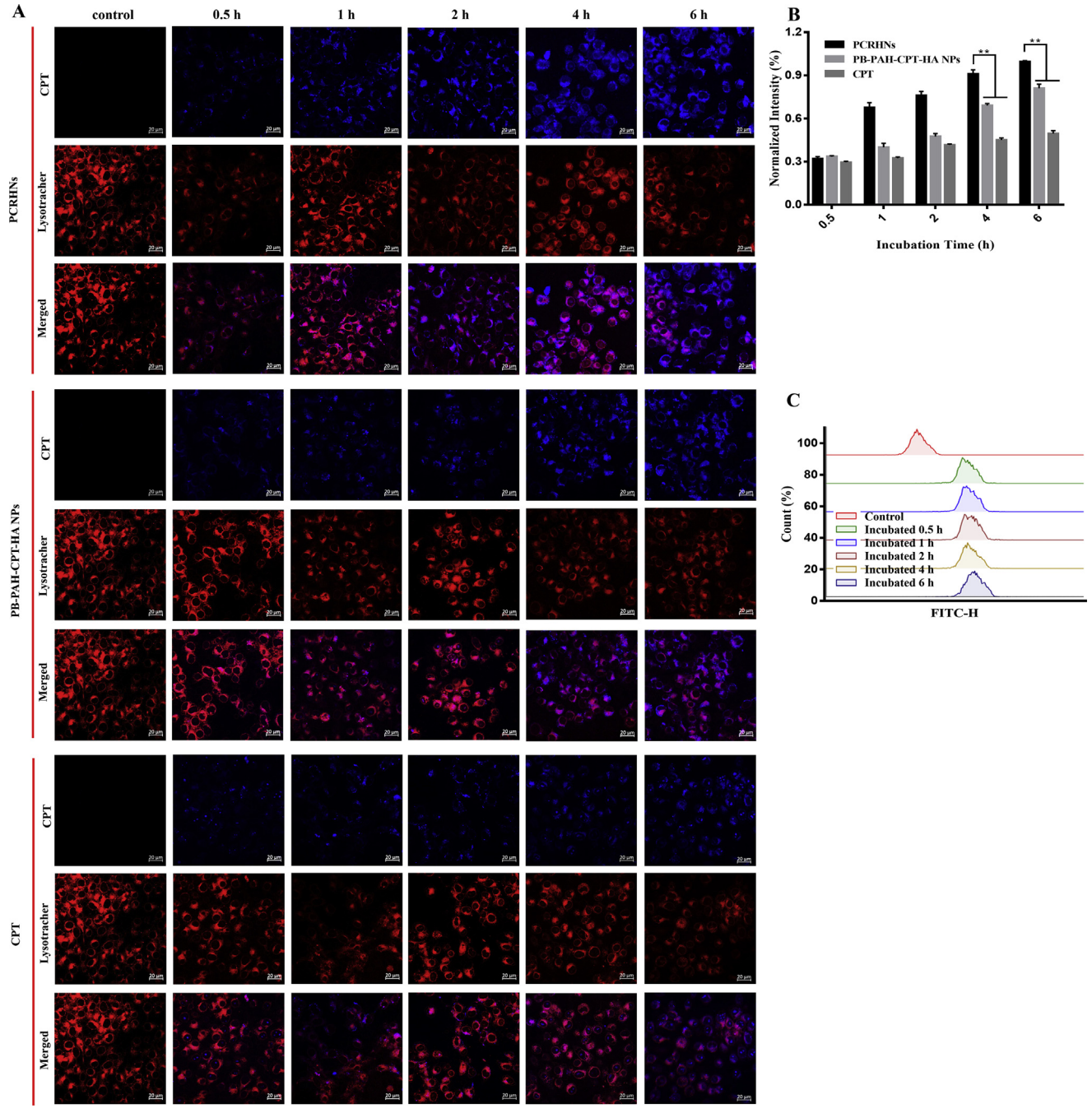

Figure 4 (A) CLSM images of 4T1 cells after incubation with CPT, PB-PAH-CPT-HA NPs, or PCRHNs (20.0 μg/mL CPT-equivalent dosage) with varying time intervals. The endosomes and lysosomes were stained with Lysotracker Red (red channel), and blue channel fluorescence emission originated from CPT moieties; scale bar = 20 μm. (B) Normalized fluorescence intensity (blue channel) of 4T1 cells was quantified from CLSM observations. (C) Flow cytometric analysis recorded for 4T1 cells incubation with FITC-PCRHNs with varying time intervals, as determined by FITC channel. Data were represented as mean ± standard deviation, $n = 3$, $^{**}P < 0.01$.

compared with the saline group (a), which demonstrated that the laser and PB NPs alone had no effect the expression of HSP70 in cancer cells. However, in the CPT (d) and PCRHNs (e) groups, the relative HSP70 level was reduced dramatically to 0.58 and 0.61, respectively, compared with the saline group (a), indicating that CPT can down-regulate the expression of HSP70, which is consistent with previous literature[72–74]. In addition, compared with the saline group (a), the expression level of HSP70 in the PCRHNs + laser group (h) was significantly down-regulated to 0.45 even under the photothermal induction condition, which demonstrated that the hyperthermia-induced upregulation of heat shock protein 70 in the tumor cells could be inhibited by CPT. The similar results also occurred in the CPT group (d′), PCRHNs group (e′), and PCRHNs + laser group (h′) incubation at 40 °C, where the relative level of HSP70 was lower than that of in the saline group incubation at 40 °C (a′).

The MTT assay was used to determine the relative viabilities of 4T1 cells under different treatments (Fig. 5E). Comparing the cell

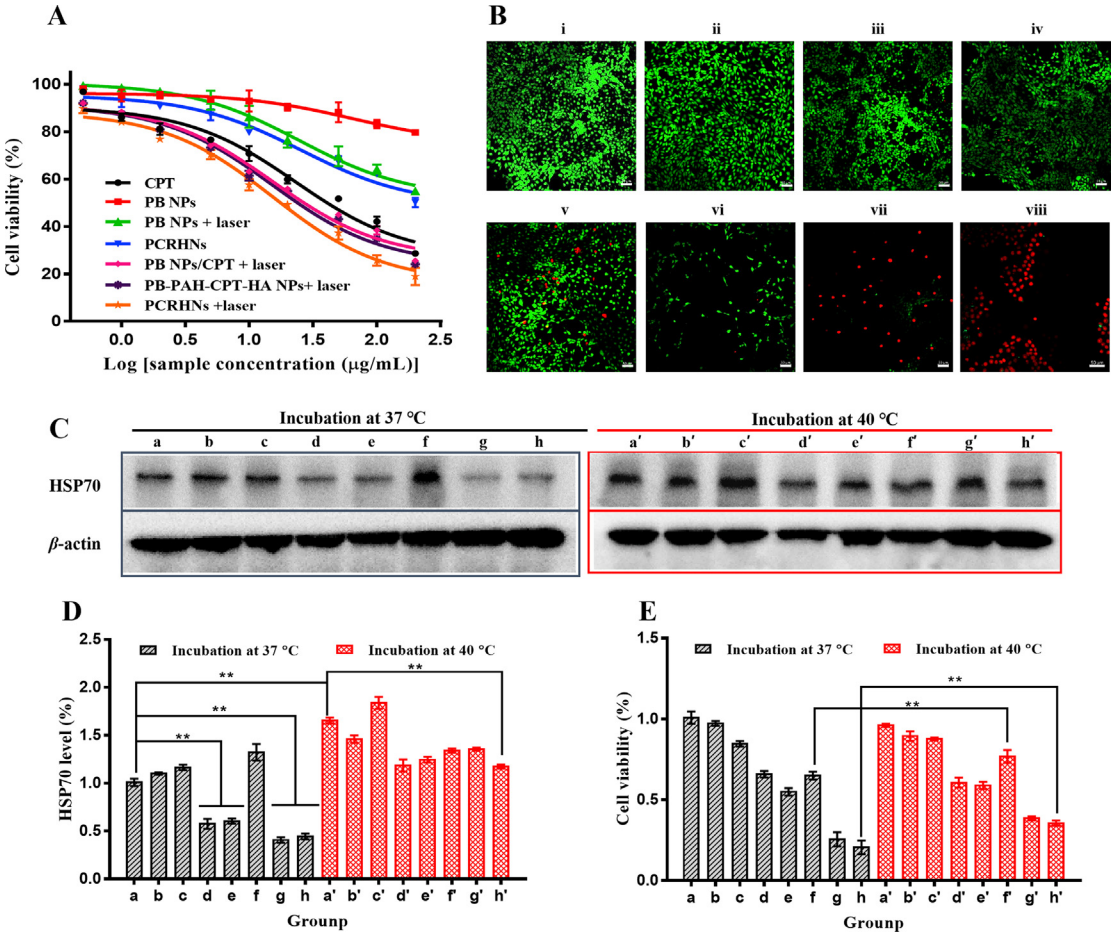

Figure 5 (A) *In vitro* cytotoxicity determined by MTT assay against 4T1 cells with different treatments. (B) CLSM images of Calcein-AM/PI costaining of 4T1 cells after with different treatments (i: saline; ii: saline + laser; iii: CPT (20.0 μg/mL); iv: PCRHNs (200.0 μg/mL); v: PB NPs + laser (160.0 μg/mL); vi: PB NPs/CPT + laser (180.0 μg/mL, 8:1, *m*/*m*); vii: PB-PAH-CPT-HA NPs + laser (200.0 μg/mL); and viii: PCRHNs + laser (200.0 μg/mL)), scale bar = 50 μm. Representative Western blotting of HSP70 expression (C) and gray analysis (D), and (E) the viability of the 4T1 cells under different conditions (a: saline; b: saline + laser; c: PB NPs (160.0 μg/mL); d: CPT (20.0 μg/mL); e: PCRHNs (200.0 μg/mL); f: PB NPs + laser (160.0 μg/mL); g: PB NPs/CPT + laser (180.0 μg/mL, 8:1, *m*/*m*); h: PCRHNs + laser (200.0 μg/mL); a′: saline under incubation at 40 °C; b′: saline + laser under incubation at 40 °C; c′: PB NPs (160.0 μg/mL) under incubation at 40 °C; d′: CPT (20.0 μg/mL) under incubation at 40 °C; e′: PCRHNs (200.0 μg/mL) under incubation at 40 °C; f′: PB NPs + laser (160.0 μg/mL) under incubation at 40 °C; g′: PB NPs/CPT + laser (180.0 μg/mL, 8:1, *m*/*m*) under incubation at 40 °C; h′: PCRHNs + laser (200.0 μg/mL) under incubation at 40 °C). Data were represented as mean ± standard deviation, $n = 3$, $^{**}P < 0.01$.

viability of photothermal treatment groups (f and f′; h and h′), it was found that the cell viability of the same treatment at 40 °C was higher than that at 37 °C, indicating that up-regulating the expression of HSP70 can reduce the tumor's susceptibility to the PB NPs-mediated PTT. In conclusion, the active CPT drugs released by PCRHNs can not only exert the efficacy of chemotherapy, but also down-regulate the expression of HSP70 to enhance the susceptibility of tumor cells to the PB NPs-mediated PTT. This conclusion reasonably explains the chemo-photothermal synergistic therapy mediated by PCRHNs *in vitro*, and more potential mechanisms need to be further studied.

3.7. *Pharmacokinetic profile and tissue distribution of PCRHNs*

After PEGylation, conjugation of cRGD and HA, PCRHNs should have good systemic circulation and tumor-targeting ability. We investigated the blood circulation time of PCRHNs, PB-PAH-CPT-HA NPs, and CPT through pharmacokinetic study. After the intravenous (i.v.) injection of PCRHNs, PB-PAH-CPT-HA NPs, or CPT into the healthy Sprague−Dawley (SD) rats, the CPT content in the blood of the CPT-treated group dropped dramatically in 4 h, and only 1.18% injection dose of CPT was left in plasma at 8 h. Moreover, the concentration of circulating CPT decreased to almost 0 after 12 h post-injection. In the PCRHNs and PB-PAH-CPT-HA NPs-treated groups, the CPT content was not significantly changed, and only low levels were detected within 48 h (Fig. 6A-1). These results indicated that PCRHNs maintain high stability in the bloodstream, thus reducing the distribution of CPT in other tissues. However, after GSH treatment of the plasma, the CPT content in the blood of the PCRHNs and PB-PAH-CPT-HA NPs-treated groups also had a significant drop at 4 h, but both were higher than that in the CPT-group (Fig. 6A-2). Even at 48 h, the CPT content in the PCRHNs-treated group remained at 4.76% injection dose. These results indicate that PCRHNs have long-lasting circulation due to the combination of PEGylation and conjugation with HA.

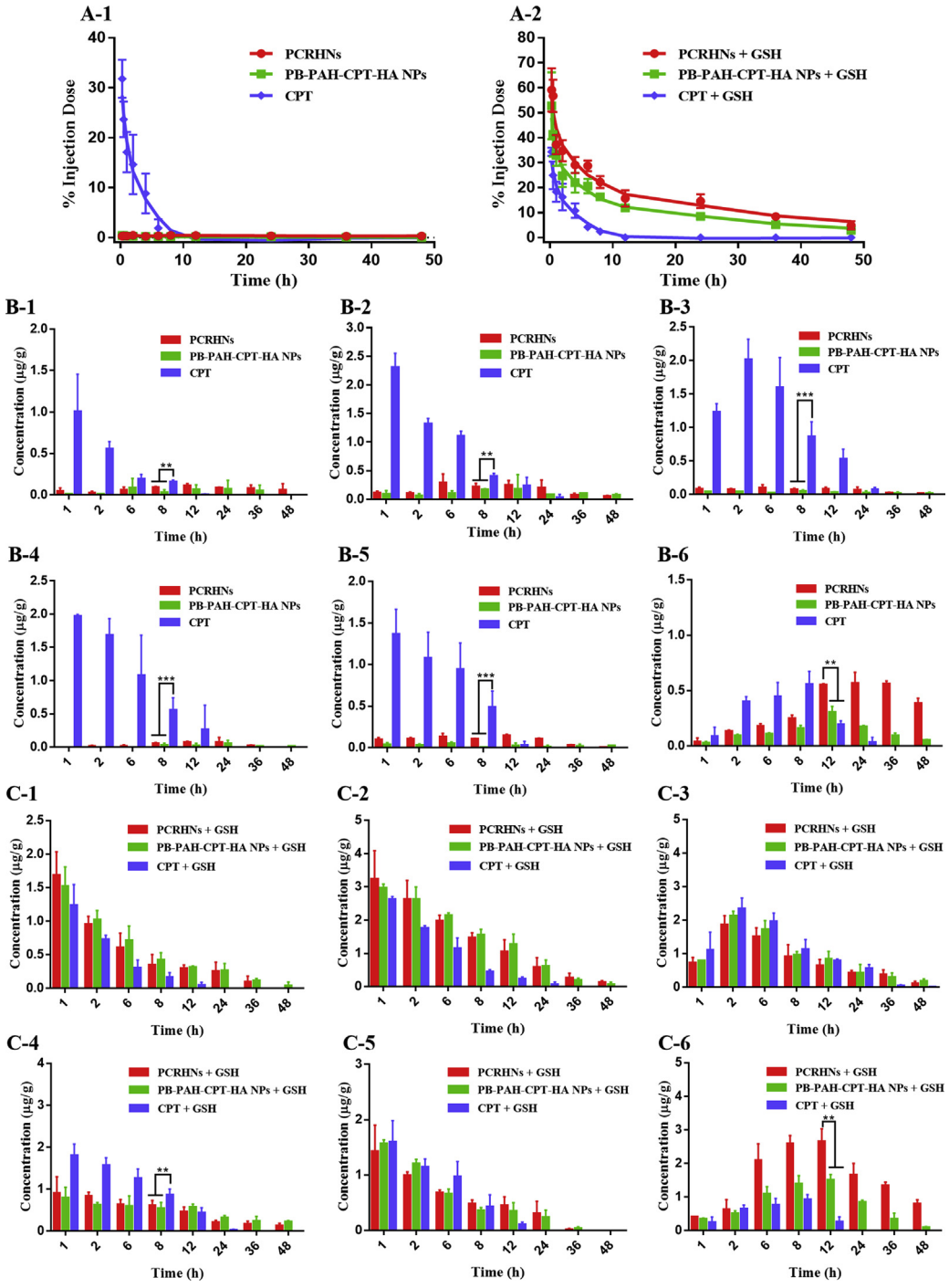

Figure 6 Plasma concentration−time profiles of CPT after i.v. injection of PCRHNs, PB-PAH-CPT-HA NPs, or CPT; Plasma was treated without GSH (A-1), or with 10.0 mmol/L GSH (A-2); Calculated as percentage of injected dose remaining in the blood. The CPT concentrations in different organs at different time points after i.v. injection of PCRHNs, PB-PAH-CPT-HA NPs, or CPT; (B-1) heart, (B-2) liver, (B-3) spleen, (B-4) lung, (B-5) kidney, and (B-6) tumor homogenate was treated without GSH; (C-1) heart, (C-2) liver, (C-3) spleen, (C-4) lung, (C-5) kidney, and (C-6) tumor homogenate was treated with 10.0 mmol/L GSH. Data were represented as mean ± standard deviation, $n = 3$, $^{**}P < 0.01$, $^{***}P < 0.005$.

Furthermore, we established a 4T1 cancer model in BALB/c mice to investigate the tissue distribution of PCRHNs *in vivo*. The contents of CPT in the heart, liver, spleen, lungs, kidneys, and tumor after i.v. injection of PCRHNs, PB-PAH-CPT-HA NPs, and CPT are shown in Fig. 6B. The CPT contents of primary organs (heart, liver, spleen, lungs, and kidneys) in the PCRHNs and PB-PAH-CPT-HA NPs-treated groups were much lower than in the CPT-treated group within 8 h after administration (Fig. 6B-1−B-5). Nevertheless, after GSH treatment of the tissue homogenates, it was found that the content of CPT in the lung tissue of the PCRHNs and PB-PAH-CPT-HA NPs-treated groups were lower than that of the CPT-treated group, but there was no significant

difference in other primary organs (Figs. 6C-1−C-5). These results indicated that PCRHNs and PB-PAH-CPT-HA NPs were also distributed in the live tissues, but due to the low content of GSH in normal tissues, the PCRHNs and PB-PAH-CPT-HA NPs would not release too much CPT, which reduced the side effects of CPT. However, the CPT content in the tumor tissue of the PCRHNs-treated mice reached 0.5 μg/g at 12 h and remained at a relatively high level compared with the CPT- and PB-PAH-CPT-HA NPs-treated groups until 48 h (Fig. 6B-6). These results indicate that PCRHNs have good-tumor targeting and CPT-releasing ability in tumor sites. In addition, after GSH treatment of the tumor tissue homogenates, the content of CPT was reached 2.5 μg/g at 12 h in the PCRHNs-treated group (Fig. 6C-6), which was about 5 times the amount before GSH treatment, indicating that more PCRHNs were enriched in the tumor tissue, which indicated the possibility of long-term release of CPT.

3.8. *Photoacoustic imaging and photothermal conversion in vivo*

Before evaluating the overall anticancer performance of the nanosystem on live animal models and taking advantage of the strong NIR absorbance of PCRHNs, PAI and photothermal conversion *in vivo* was carried out. Combining the long circulation and active targeting of PCRHNs *in vivo*, we could deduce that the tumor sites treated with PCRHNs have significantly enhanced photoacoustic signals and photothermal conversion effects. For the PAI study, we investigated the PA signal of the PCRHNs with different concentrations *in vitro* using a MSOT small animal scanner. The results shown in Supporting Information Fig. S12 demonstrated that the PCRHNs had good linear correlation with the concentration in the range of 1.0−100 μg/mL, which further indicated that PCRHNs has great potential in PAI. Thereafter, we used the PAI system to investigate the enrichment of PCRHNs in tumor sites (Fig. 7A). The intrinsic photoacoustic signals were rather weak in the tumor before injection, and the tumor vasculatures clearly lightened up right after i.v. injection of PCRHNs owing to the circulation of nanoparticles in the blood. Over time, the photoacoustic signals became stronger and dispersed throughout the whole tumor. During the monitoring process, the PAI signal of the tumors treated with PCRHNs was significantly higher than that of the tumors treated with PB-PAH-CPT-HA NPs and reached a maximum at 6 h (Fig. 7B), indicating that PCRHNs have good tumor targeting and accumulation, and can be used as a promising candidate agent for PAI; Subsequently, the PAI signal of the tumors treated with PCRHNs was relatively decreased at 24 h, indicating that PB NPs are biodegradable *in vivo*.

Next, the *in vivo* photothermal conversion efficacy of PCRHNs in the tumor site was examined. The NIR laser illumination was implemented 6 h after the i.v. injection of PCRHNs to maximize the therapeutic effect according to the results of PAI. The changes in tumor temperature were recorded using an IR thermal camera during the entire PTT course (Fig. 7C). As illustrated in Fig. 7D, the tumor temperature in the PCRHNs + laser group rapidly

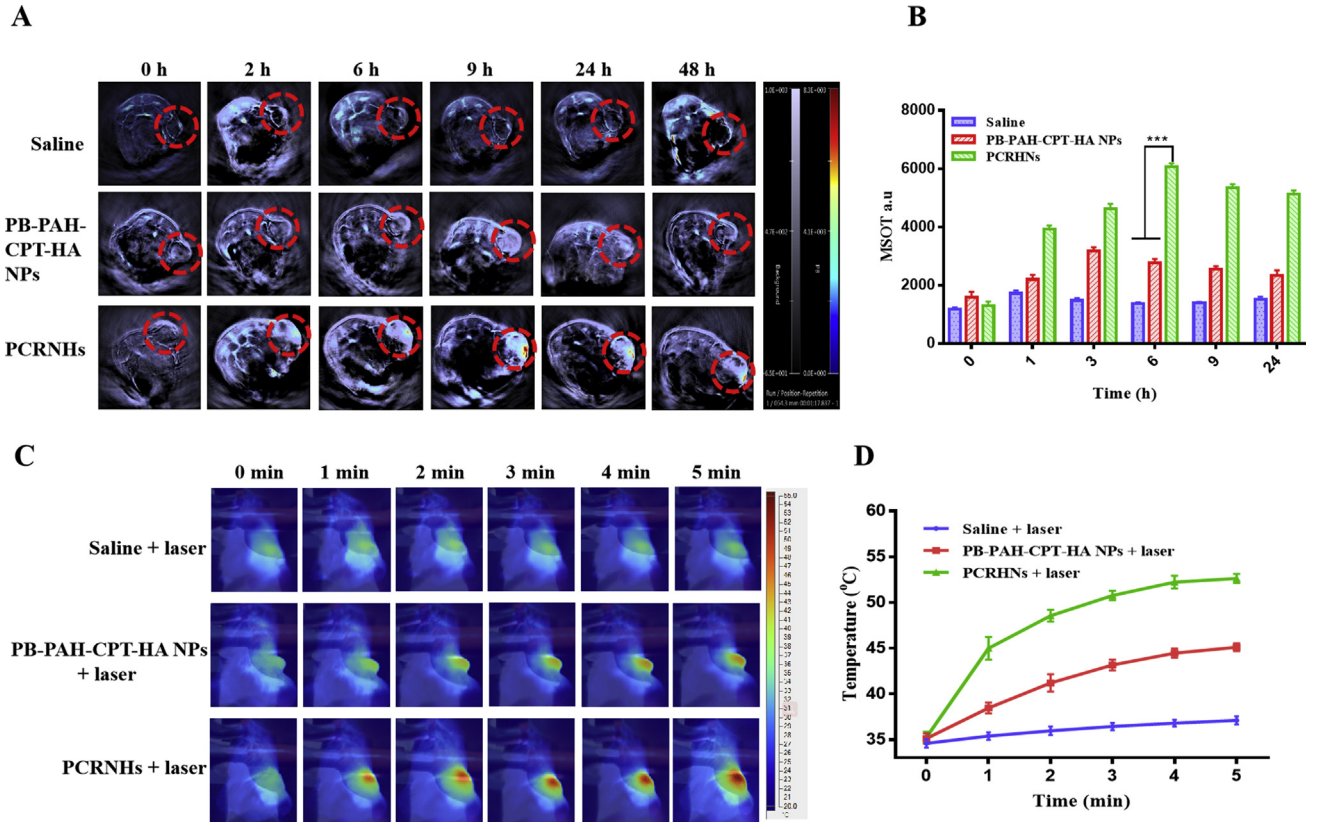

Figure 7 PAI (A) and PA intensity (MSOT a.u) (B) of 4T1 tumor-bearing mice taken at different time points after i.v. injection with saline (control group), PB-PAH-CPT-HA NPs or PCRHNs; The images represent the transverse sections of the mice during PAI, the tumors were marked in red circles. Photothermal conversion of PB-PAH-CPT-HA NPs and PCRHNs *in vivo*; (C) IR thermographic images of 4T1 tumor-bearing mice under the 808 nm laser irradiation taken at different time points, and (D) the curves of surface temperatures of the tumor site during irradiation; The laser power density was 1.0 W/cm^2 for 5 min. Data were represented as mean ± standard deviation, $n = 3$, $^{***}P < 0.005$.

increased to 52.8 °C after 5 min of NIR laser radiation (808 nm, 1.0 W/cm^2), whereas the tumor temperature in the PB-PAH-CPT-HA NPs + laser group increased relatively slowly—after 5 min of NIR laser radiation, it reached 44.6 °C. In contrast, the saline + laser group showed only a minimal tumor temperature increase (less than 5 °C), which confirmed the low biological invasiveness of an NIR laser at 808 nm. These results are attributed to the targeting effect of cRGD, which facilitated the accumulation of the nanoparticles in tumor tissues. It is also concluded that PCRHNs have good photothermal conversion effect *in vivo.*

3.9. *Tumor growth inhibition mediated by PCRHNs in vivo*

3.9.1. *In vivo antitumor effect*

The anticancer performance of PCRHNs *in vivo* was further evaluated using 4T1 tumor-bearing BALB/c mice. When the tumor volume reached about 150 mm^3, the mice were divided and administered different treatments. Body weight, and tumor volume were recorded every other day. As shown in Fig. 8C, mice in the PB NPs + laser (V) and PB NPs/CPT + laser (VI) groups that contained free PB NPs showed significant weight loss; although

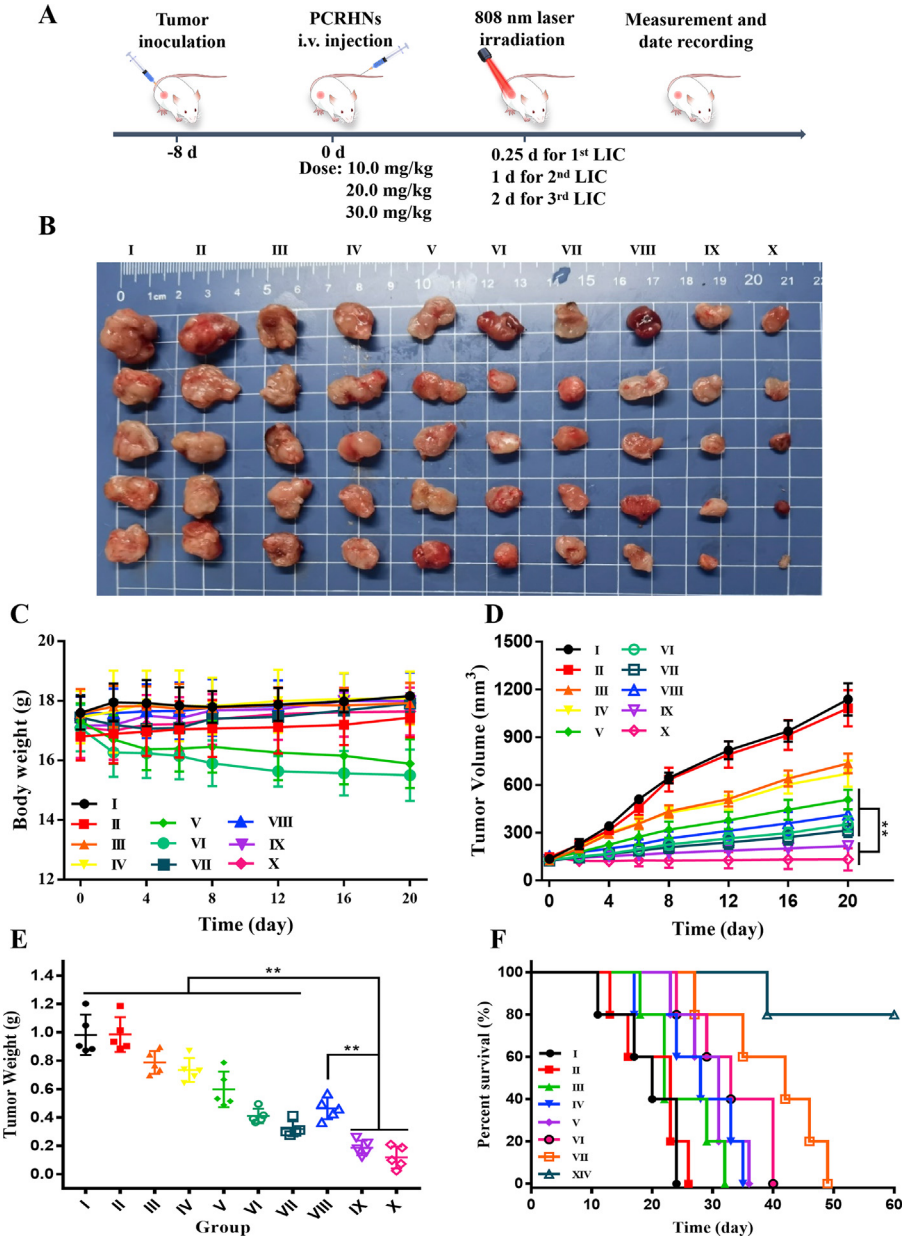

Figure 8 Anticancer performance of PCRHNs in chemo-photothermal combinational therapy of breast cancer. (A) Administration route. (B) Photographs of subcutaneous tumors in each group (I: saline group; II: saline + laser group; III: CPT group (2.0 mg/kg); IV: PCRHNs group (20.0 mg/kg); V: PB NPs + laser group (16.0 mg/kg); VI: PB NPs/CPT + laser group (18.0 mg/kg, 8:1, *m*/*m*); VII: PB-PAH-CPT-HA NPs + laser group (20.0 mg/kg); VIII: PCRHNs + laser group (10.0 mg/kg, low-dose); IX: PCRHNs + laser group (20.0 mg/kg, medium-dose); X: PCRHNs + laser group (30.0 mg/kg, high-dose); each group comprised 5 mice). (C) Body weight of the mice in each group. (D) Growth curves of tumor in the mice in each group. (E) Tumor weight in each group. (F) Survival curves of the mice (XIV: PCRHNs + laser group (20.0 mg/kg, medium-dose, three LICs)). Data were represented as mean ± standard deviation, $n = 5$, $^{**}P < 0.01$.

PB NPs have been approved by the FDA for clinical use on patients for many years, adverse reactions can also occur at large doses. However, there was no noticeable change in the body weight of mice in the PCRHNs + laser groups (VIX−X), suggesting that the experimental treatments were well tolerated. The results of tumor growth suppression (Fig. 8D) demonstrated that the 4T1 tumors treated with saline + laser (II) grew rapidly, illustrating that NIR laser irradiation had no effect on tumor growth. The tumor growth was relatively fast in the CPT (III) and PCRHNs (IV) groups, indicating that the administration of CPT or PCRHNs alone could not effectively inhibit tumor growth. Meanwhile, the tumor growth could not be inhibited by PB NPs + laser (V), this may be mainly ascribed to that the insufficient tumor growth inhibition by PB NPs-mediated photothermal therapies[53]. Through the combination of chemotherapy and PTT mediated by PB NPs/CPT (VI), significantly enhanced tumor inhibition was achieved compared with the CPT (III) and PB NPs + laser (V) groups. However, because of the deficiency of tumor targeting, the PB NPs/CPT + laser (VI) and PB-PAH-CPT-HA + laser (VII) groups showed lower *in vivo* anticancer potency compared with the PCRHNs + laser (20.0 mg/kg) group (IX). Similarly, the free CPT group (III) showed less anticancer activity than the PCRHNs group (IV). Additionally, the dose of PCRHNs was investigated. There was no significant difference in the anticancer activity between the medium-dose group (IX) and the high-dose group (X), but both doses performed significantly better than the low-dose group (VIII) (Fig. 8E). In addition, the tumor weights of the mice treated with different treatments and the photographs

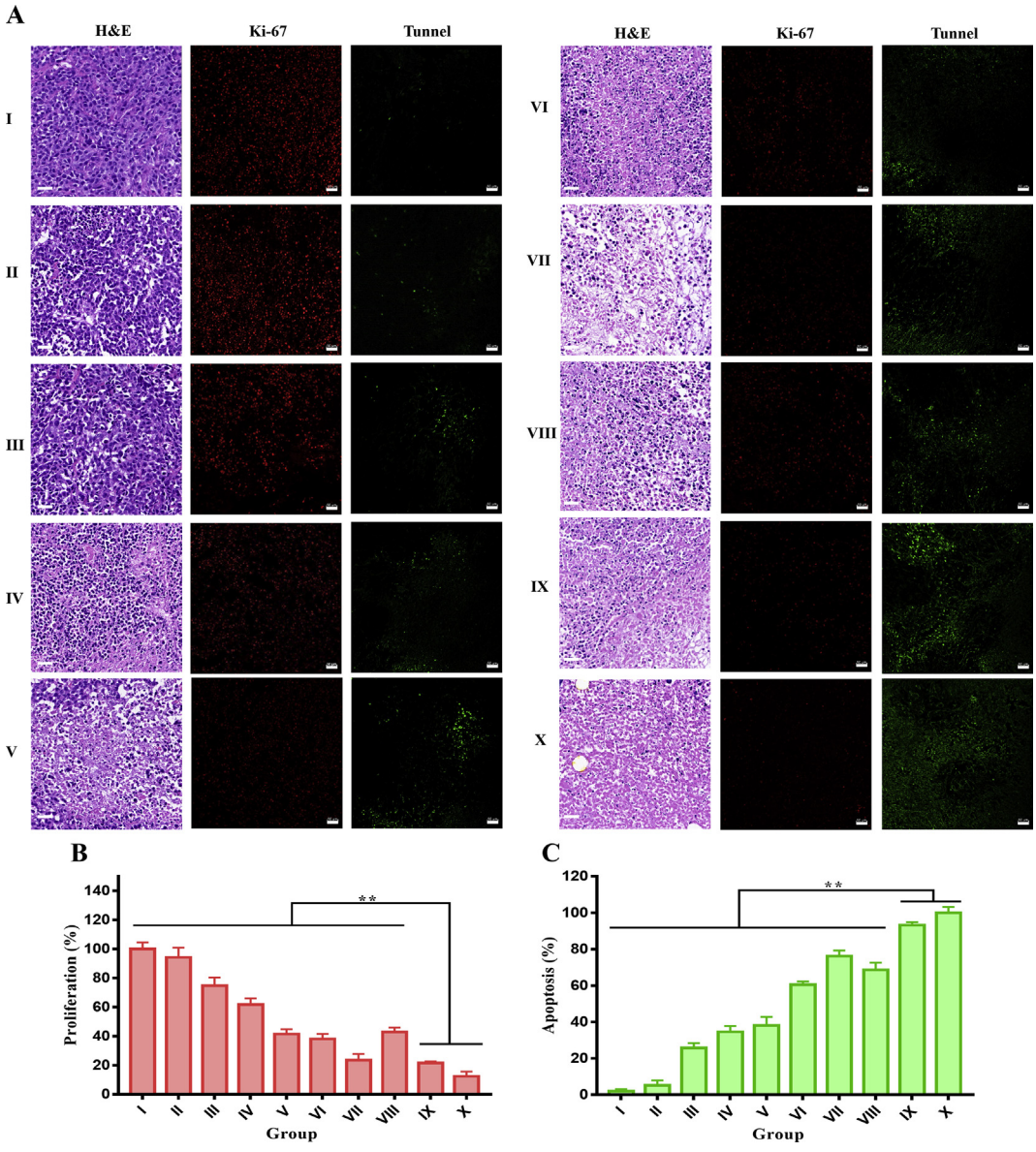

Figure 9 (A) Representative H&E, Ki-67, and TUNEL staining of tumor in each group (I: saline group; II: saline + laser group; III: CPT group (2.0 mg/kg); IV: PCRHNs group (20.0 mg/kg); V: PB NPs + laser group (16.0 mg/kg); VI: PB NPs/CPT + laser group (18.0 mg/kg, 8:1, *m*/*m*); VII: PB-PAH-CPT-HA NPs + laser group (20.0 mg/kg); VIII: PCRHNs + laser group (10.0 mg/kg, low-dose); IX: PCRHNs + laser group (20.0 mg/kg, medium-dose); X: PCRHNs + laser group (30.0 mg/kg, high-dose)), scale bar = 50 μm. Quantitative fluorescence analysis of the tumor cell proliferation (B), and tumor cell apoptosisa (C) in each group. Data were represented as mean ± standard deviation, $n = 5$, $^{**}P < 0.01$.

of the tumors eviscerated from the mice further demonstrated the efficiency of the chemotherapy/PTT cotherapy with PCRHNs in tumor growth inhibition *in vivo* (Fig. 8B and E).

Extending from the analysis on the tumor weight changes, the extracted tumors were further sectioned for histological analysis by the hematoxylin and eosin (H&E) staining. A significant area of cancer cell remission and no noticeable organ damage or inflammatory lesion were observed in all major organs of mice receiving PCRHNs injection and photothermal treatment (IX and X), preliminarily verifying that PCRHNs rendered no obvious toxic side effects to the mice in the short term at our tested dose (Fig. 9A and Supporting Information Fig. S13). The proliferation and apoptosis of tumors *in vivo* were further evaluated by immunofluorescence staining (Ki-67 and TUNEL). The proliferation and apoptosis results of the tumor cells with different treatments *in vivo* further demonstrated that PCRHNs are a promising candidate for chemo-photothermal synergistic therapy of breast cancer (Fig. 9A–C). To explore the mechanism of PCRHNs-mediated chemo-photothermal synergistic therapy *in vivo*, tumors were eviscerated from the mice 48 h after the administration, and the extracted tumors were further sliced into sections for the immunofluorescence staining of HSP70. As shown in Fig. 10A and B, the expression level of HSP70 in the PB NPs + laser group (V) was 1.36 times that of the saline group (I), indicating that PTT could enhance the expression of HSP70 in the tumor tissue. However, compared with the saline group (I), the expression levels of HSP70 in the CPT (III), and PCRHNs (IV) groups were down-regulated, indicating that CPT can down-regulate the expression of HSP70 in tumor cells *in vivo*. In addition, compared with the saline group (I) and CPT group (III), the expression level of HSP70 in the PCRHNs + laser group (IX) was significantly down-regulated even under the photothermal induction condition, which may be related to several reasons: first, PCRHNs have good tumor targeting and

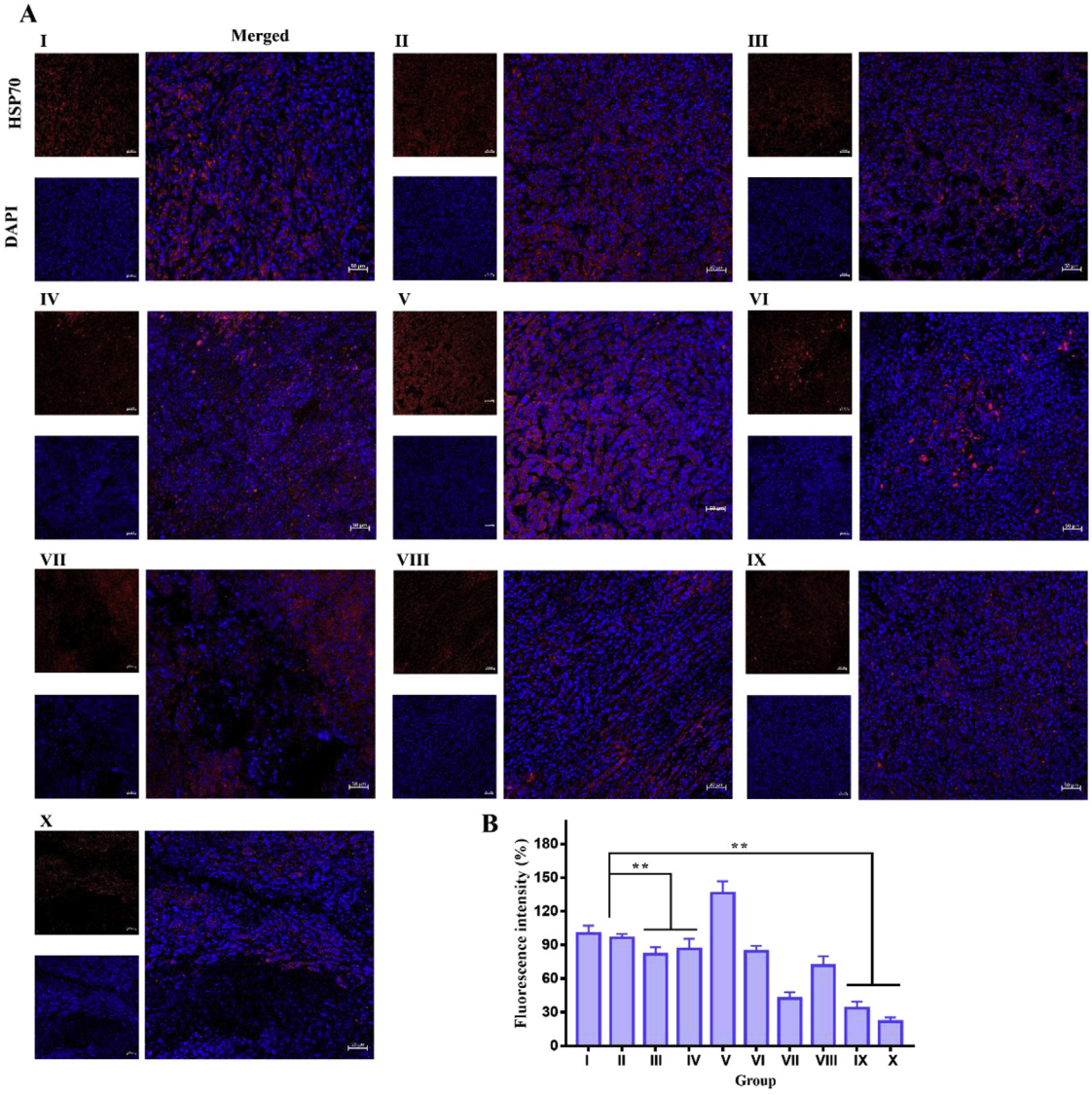

Figure 10 (A) Representative immune-fluorescence imaging of HSP70 in tumors after different treatment (I: saline group; II: saline + laser group; III: CPT group (2.0 mg/kg); IV: PCRHNs group (20.0 mg/kg); V: PB NPs + laser group (16.0 mg/kg); VI: PB NPs/CPT + laser group (18.0 mg/kg, 8:1, *m*/*m*); VII: PB-PAH-CPT-HA NPs + laser group (20.0 mg/kg); VIII: PCRHNs + laser group (10.0 mg/kg, low-dose); IX: PCRHNs + laser group (20.0 mg/kg, medium-dose); X: PCRHNs + laser group (30.0 mg/kg, high-dose); Blue channel: cell nucleus; Red channel: HSP70 protein expressing region), scale bar = 50 μm. (B) Quantitative fluorescence analysis of the HSP70 expression in each group. Data were represented as mean ± standard deviation, $n = 5$, $^{**}P < 0.01$.

accumulation, thus providing more CPT to tumor tissue; Second, the active CPT drugs released by PCRHNs can not only exert the efficacy of chemotherapy, but also down-regulate the expression of HSP70 to enhance the susceptibility of tumor cells to the PB NPs-mediated PTT, thereby achieving synergistic antitumor activity, which reasonably explains the obvious ablation of tumor tissues in the PCRHNs + laser group after PTT. However, there are other explanations for the synergistic effect of chemotherapy combined with PTT *in vivo*[76,77], so more potential mechanisms behind PCRHNs-mediated chemo-photothermal synergistic therapy need to be further investigated.

3.9.2. *Multiple photothermal therapy cycles*

According to the previous research results of our team, multiple PTT cycles after a single administration have better therapeutic effects than a single PTT cycle[78]. Next, the PTT cycles were investigated. The experimental groups of low, medium and high doses of PCRHNs combined with different PTT cycles were set. The temperature change of the tumor tissue was recorded during the entire PTT course. According to the temperature curves (Fig. 11A−C), it was found that the increase of temperature was positively correlated with the dosage of PCRHNs; In the high-dose group (30.0 mg/kg), the temperature eventually increased by 19.6 °C in the first laser irradiation cycle (LIC), while in the low-dose group (10.0 mg/kg), the temperature only increased by 10.2 °C in the first LIC; At the same dose, the temperature change of the first and second LIC were basically the same, while the temperature increase of the third LIC was reduced because the PB NPs are biodegradable. The tumor volume changes and tumor weight in each group were shown in Fig. 11D−H. In the low-dose groups (VIII, XI, and XII), the tumor growth was not effectively inhibited, and there was no significant difference in the therapeutic effect with one or more LIC; In the medium-dose groups (IX, XIII, and XIV) and high-dose groups (X, XV, and XVI), the tumor growth was effectively suppressed after first LIC, part of the tumor tissue was eliminated after two LICs, and the tumor tissue was completely ablated without recurrence after three LICs. Therefore, multiple PTT cycles after a single administration of PCRHNs can increase the therapeutic effect. During the experimental period, there was no significant change in the body weight of all mice (Fig. 11I). There were also no observable changes in tissue morphology, hemorrhage, and inflammatory cell infiltration in H&E stained sections of the heart, liver, spleen, lung, and kidney of all treated groups (Supporting Information Fig. S14), confirming that multiple PTT cycles rendered no obvious toxic side effects on mice. Overall, the medium dose (20.0 mg/kg) with three LICs was selected as the treatment regimen for the animal survival

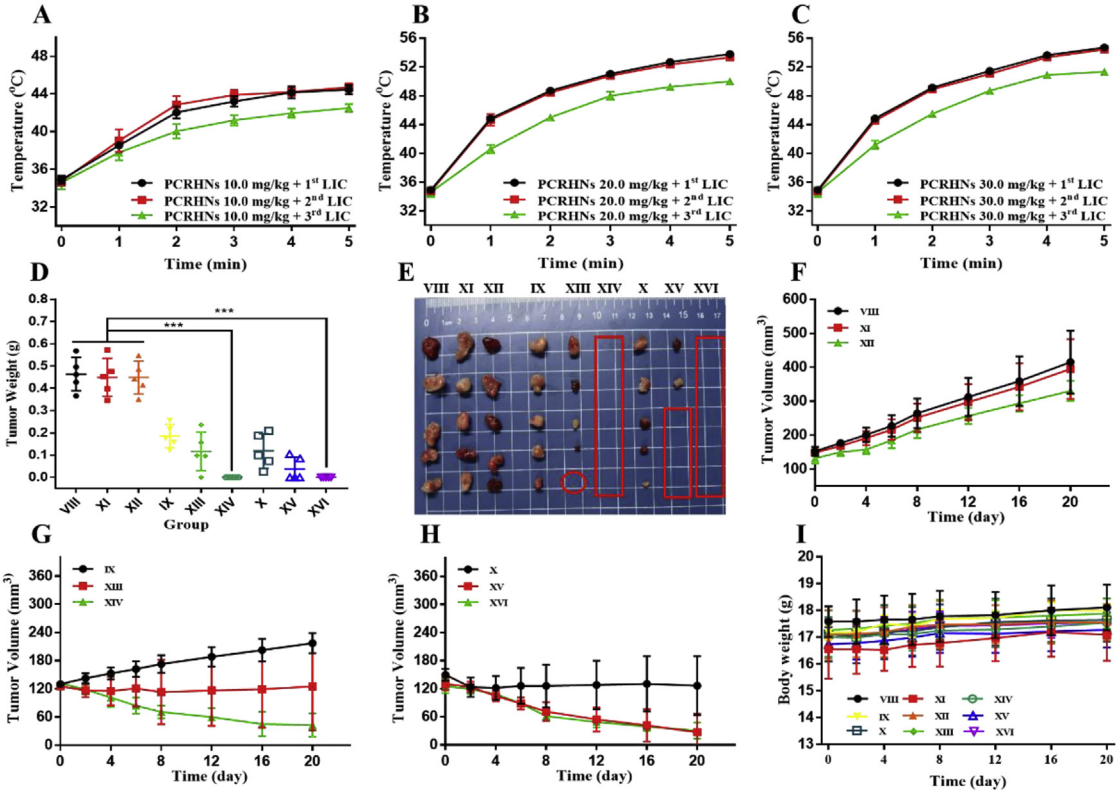

Figure 11 Multiple photothermal effects of PCRHNs in 4T1-tumor-bearing mice. (A)−(C) The curves of surface temperatures of the tumor site during irradiation, the 808 nm laser power density was 1.0 W/cm^2 for 5 min (1st LIC: the first laser irradiation cycle; 2nd LIC: the second laser irradiation cycle; 3rd LIC: the third laser irradiation cycle; each group comprised 5 mice). (D) Tumor weights in each group (VIII: PCRHNs + laser group (10.0 mg/kg, low-dose); IX: P CRHNs + laser group (20.0 mg/kg, medium-dose); X: PCRHNs + laser group (30.0 mg/kg, high-dose); XI: PCRHNs + laser group (10.0 mg/kg, low-dose, two LICs); XII: PCRHNs + laser group (10.0 mg/kg, low-dose, three LICs); XIII: PCRHNs + laser group (20.0 mg/kg, medium-dose, two LICs); XIV: PCRHNs + laser group (20.0 mg/kg, medium-dose, three LICs); XV: PCRHNs + laser group (30.0 mg/kg, high-dose, two LICs); XVI: PCRHNs + laser group (30.0 mg/kg, high-dose, three LICs)). (E) Photographs of subcutaneous tumors in each group. (F)−(H) Growth curves of tumor in the mice in each group. (I) Body weight of the mice in each group. Data were represented as mean ± standard deviation, $n = 5$, $^{***}P < 0.005$.

study. The number of living mice were recorded every other day. As shown in Fig. 9F, the survival of the mice treated with chemotherapy/PTT cotherapy by PCRHNs was greatly prolonged, and the tumor recurrence rate within 60 days is very low (20.0%).

3.10. Toxicity of PCRHNs in vivo

The potential toxicity of PCRHNs *in vivo* was investigated. Healthy BALB/c mice were i.v. injected with PB NPs/CPT (8:1, *m*/*m*) and PCRHNs at a dose of 40.0 mg/kg, which was 2 times the amount of the imaging/therapy dose. Neither mouse death nor noticeable abnormal behavior was observed for those mice receiving a high dose of PCRHNs. However, the mice in the PB NPs/CPT group showed malaise and occasional convulsions, and all mice died within 1 day. The complete blood panel tests and serum biochemistry assays were carried out on PCRHNs injected mice at Days 1, 7, and 30 post injection. All parameters of complete blood tests of the PCRHNs-treated mice were in the normal range; white blood cells (WBC), red blood cell (RBC), platelets (PLT), and hemoglobin (HGB) were selected as representatives (Supporting Information Table S3). The liver function indexes, including alanine aminotransferase (ALT), alkaline phosphatase (ALP), and aspartate aminotransferase (AST), as well as kidney function indicator uric acid (UA), urea (UREA), and creatinine (CREA), were all measured to be normal (Supporting Information Table S3), suggesting no hepatic or kidney dysfunction induced by PCRHNs. Additionally, the major organs, including the heart, liver, spleen, lungs, and kidneys, were collected and stained with H&E for histology analysis after 30 days of intravenous injection; no obvious tissue damage of inflammatory lesions was found in any major organs, and no abnormal behavior of the PCRHNs-treated mice was observed (Fig. S15). All of these results suggested that PCRHNs have negligible toxicity *in vivo*.

4. Conclusions

In summary, we have successfully developed a tumor-targeted/reduction-triggered composite multifunctional nanoparticle system (PCRHNs) for breast cancer chemo-photothermal combinational therapy. PCRHNs was prepared by grafting an amphiphilic block copolymer (COOH-PEG_{4000}-$PssCPT_9$) onto PB NPs, and then modifying it with tumor-targeting polymer (NHS-PEG_{5000}-cRGD) and HA. PCRHNs exhibited nano-sized structure (~151.4 nm) with good monodispersity, high load efficiency of CPT (9.2 ± 0.3%), triggered CPT release in response to reduction environment, and excellent photothermal conversion under 808 nm laser irradiation. PCRHNs show high stability in blood circulation due to their nanoscale particle size, PEGylation and HA modification their pharmacokinetic profile; Therefore, PCRHNs can efficiently accumulate in tumor sites based on a combination of both passive targeting and cRGD-mediated active targeting *in vivo* PAI and biodistribution analysis. In addition, the PAI results provide the optimal time point (6 h after i.v. injection) for PTT *in vivo* to achieve highly effective tumor destruction, and multiple PTT cycles after a single administration can kill tumor tissue to a greater extent. Moreover, the active CPT drugs are released in response to the intracellular GSH of tumor cells for chemotherapy, and down-regulate the expression of HSP70 to enhance the tumor's susceptibility to the PB NPs-mediated PTT. The *in vitro* and *in vivo* results demonstrated that PCRHNs possess significantly synergistic antitumor effects with reduced systemic toxicity, and the tumor recurrence rate within 60 days is very low (20.0%). In conclusion, PCRHNs would be a promising therapeutic way for breast cancer targeted therapy.

Acknowledgments

This work was supported by the National Natural Science Foundation of China (NSFC31930067, NSFC31771096, and NSFC31700869), the National Key Research and Development Program of China (2017YFC1103502), the 135 Project for Disciplines of Excellence, West China Hospital, Sichuan University (ZYGD18002, China), and the Post-Doctor Research Project, West China Hospital, Sichuan University (No.19HXBH099, China). The authors thank Dr. Zhongqin Yan from the West China School of Pharmacy, Sichuan University, China for the PAI observation and analysis of the data.

Author contributions

Yun Yang and Zhiyong Qian designed the research. Yun Yang, Danrong Hu, Yi Lu, Bingyang Chu, Xinlong He, and Yu Chen carried out the experiments and performed data analysis. Yao Xiao, Chengli Yang, Kai Zhou, and Liping Yuan participated part of the experiments. Yun Yang and Zhiyong Qian wrote the manuscript. Yun Yang and Zhiyong Qian revised the manuscript. All of the authors have read and approved the final manuscript.

Conflicts of interest

The authors have no conflicts of interest to declare.

Appendix A. Supporting information

Supporting information to this article can be found online at https://doi.org/10.1016/j.apsb.2021.08.021.

References

1. Sung H, Ferlay J, Siegel RL, Laversanne M, Soerjomataram I, Jemal A, et al. Global Cancer Statistics 2020: GLOBOCAN estimates of incidence and mortality worldwide for 36 cancers in 185 countries. *CA Cancer J Clin* 2021;**71**:209–49.
2. Masuda N, Lee SJ, Im YH, Lee ES, Yokata I, Kuroi K, et al. Adjuvant capecitabine for breast cancer after preoperative chemotherapy. *N Engl J Med* 2007;**376**:2147–59.
3. Alberro JA, Ballester B, Deulofeu P, Fabregas R, Liombart HA. Long-term outcomes for neoadjuvant *versus* adjuvant chemotherapy in early breast cancer: meta-analysis of individual patient data from ten randomised trials. *Lancet Oncol* 2018;**19**:27–39.
4. Qu Y, Chu B, Wei X, Lei M, Hu D, Zha R, et al. Redox/pH dual-stimuli responsive camptothecin prodrug nanogels for "on-demand" drug delivery. *J Control Release* 2019;**296**:93–106.
5. Li X, Yang X, Lin Z, Wang D, Mei D, He B, et al. A folate modified pH sensitive targeted polymeric micelle alleviated systemic toxicity of doxorubicin (DOX) in multi-drug resistant tumor bearing mice. *Eur J Pharmaceut Sci* 2015;**76**:95–101.
6. Roduner E. Size matters: why nanomaterials are different. *Chem Soc Rev* 2006;**35**:583–92.
7. Zhou M, Zhang X, Xu X, Chen X, Zhang X. Doxorubicin@Bcl-2 siRNA core@shell nanoparticles for synergistic anticancer chemotherapy. *ACS Appl Bio Mater* 2018;**1**:289–97.

8. Ma W, Su H, Cheetham A, Zhang W, Wang Y, Kan Q, et al. Synergistic antitumor activity of a self-assembling camptothecin and capecitabine hybrid prodrug for improved efficacy. *J Control Release* 2017;**263**:102−11.
9. Chu B, Qu Y, He X, Hao Y, Yang C, Yang Y, et al. ROS-responsive camptothecin prodrug nanoparticles for on-demand drug release and combination of chemotherapy and photodynamic therapy. *Adv Funct Mater* 2020;**52**:2005918.
10. Hou S, Zhou S, Chen S, Lu Q. Polyphosphazene-based drug self-framed delivery system as a universal intelligent platform for combination therapy against multidrug-resistant tumors. *ACS Appl Bio Mater* 2020;**4**:2284−94.
11. Wu Y, Lv S, Li Y, He H, Ji Y, Zheng M, et al. Co-delivery of dual chemodrugs with precisely controlled, high drug loading polymeric micelles for synergistic anti-cancer therapy. *Biomater Sci* 2020;**3**:949−59.
12. Zhi D, Yang T, Justin O, Zhang S, Donnelly RF. Photothermal therapy. *J Control Release* 2020;**325**:52−71.
13. Li X, Lovell JF, Yoon J, Chen X. Clinical development and potential of photothermal and photodynamic therapies for cancer. *Nat Rev Clin Oncol* 2020;**17**:657−74.
14. Vankayala R, Hwang KC. Near-infrared-light-activatable nanomaterial-mediated phototheranostic nanomedicines: an emerging paradigm for cancer treatment. *Adv Mater* 2018;**30**:1706320.
15. Chen X, Zou J, Zhang K, Zhu J, Zhang Y, Zhu Z, et al. Photothermal/matrix metalloproteinase-2 dual-responsive gelatin nanoparticles for breastcancer treatment. *Acta Pharm Sin B* 2021;**11**:271−82.
16. Zhou J, Li M, Hou Y, Luo Z, Chen Q, Cao H, et al. Engineering of a nanosized biocatalyst for combined tumor starvation and low-temperature photothermal therapy. *ACS Nano* 2018;**12**:2858−72.
17. Tao W, Ji X, Xu X, Islam MA, Li Z, Chen S, et al. Antimonene quantum dots: synthesis and application as near-infrared photothermal agents for effective cancer therapy. *Angew Chem Int Ed* 2017;**56**:11896−900.
18. Ouyang J, Feng C, Ji X, Li L, Gutti HK, Kim NY, et al. 2D monoelemental germanene quantum dots: synthesis as robust photothermal agents for photonic cancer nanomedicine. *Angew Chem Int Ed* 2019;**58**:13405−10.
19. Cai X, Jia X, Gao W, Zhang K, Ma M, Wang S, et al. A versatile nanotheranostic agent for efficient dual-mode imaging guided synergistic chemo-thermal tumor therapy. *Adv Funct Mater* 2015;**25**:2520−9.
20. Hu K, Xie L, Zhang Y, Hanyu M, Yang Z, Nagatsu K, et al. Marriage of black phosphorus and Cu^{2+} as effective photothermal agents for PET-guided combination cancer therapy. *Nat Commun* 2020;**11**:2778.
21. Ulukan H, Swaan PW. Camptothecins—a review of their chemotherapeutic potential. *Drugs* 2002;**62**:2039−57.
22. Dai M, Xu X, Song J, Fu S, Gou M, Luo F, et al. Preparation of camptothecin-loaded PCEC microspheres for the treatment of colorectal peritoneal carcinomatosis and tumor growth in mice. *Cancer Lett* 2011;**312**:189−96.
23. Zhang H, Zhu J, Chu B, Chen L, Shi K, Zhang L, et al. Preparation, characterization and in vivo antitumor evaluation of a micellar formulation of camptothecin prodrug. *Nanosci Nanotechnol Lett* 2017;**9**:1755−66.
24. Bala V, Rao S, Boyd BJ, Prestidge CA. Prodrug and nanomedicine approaches for the delivery of the camptothecin analogue SN38. *J Control Release* 2013;**172**:48−61.
25. Wen Y, Wang Y, Liu X, Zhang W, Xiong X, Han Z, et al. Camptothecin-based nanodrug delivery systems. *Cancer Biol Med* 2017;**14**:363−70.
26. Botella P, Rivero-Buceta E. Safe approaches for camptothecin delivery: structural analogues and nanomedicines. *J Control Release* 2017;**247**:28−54.
27. Wang-Gillam A, Li C, Bodoky G, Dean A, Shan Y, Jameson G, et al. Nanoliposomal irinotecan with fluorouracil and folinic acid in metastatic pancreatic cancer after previous gemcitabine-based therapy (NAPOLI-1): a global, randomised, open-label, phase 3 trial. *Lancet* 2016;**387**:545−57.
28. Poveda A, Selle F, Hilpert F, Reuss A, Savarese A, Vergote I, et al. Bevacizumab combined with weekly paclitaxel, pegylated liposomal doxorubicin, or topotecan in platinum-resistant recurrent ovarian cancer: analysis by chemotherapy cohort of the randomized phase III AURELIA trial. *J Clin Oncol* 2015;**33**:3836−8.
29. Shi L, Hu Y, Lin A, Ma C, Zhang C, Su Y, et al. Matrix metalloproteinase responsive nanoparticles for synergistic treatment of colorectal cancer simultaneous anti-angiogenesis and chemotherapy. *Bioconjugate Chem* 2016;**27**:2943−53.
30. Yu H, He J, Lu Q, Huo D, Yuan S, Zhou Z, et al. Anti-Fas antibody conjugated nanoparticles enhancing the antitumor effect of camptothecin by activating the Fas−FasL apoptotic pathway. *ACS Appl Mater Interfaces* 2016;**8**:29950−9.
31. Hu X, Hu J, Tian J, Ge Z, Zhang G, Luo K, et al. Polyprodrug amphiphiles: hierarchical assemblies for shape-regulated cellular internalization, trafficking, and drug delivery. *J Am Chem Soc* 2013;**135**:17617−29.
32. Wang S, Yu G, Wang Z, Jacobson O, Tian R, Lin L, et al. Hierarchical tumor microenvironment-responsive nanomedicine for programmed delivery of chemotherapeutics. *Adv Mater* 2018;**30**:1803926.
33. Lee MH, Yang Z, Lim CW, Lee YH, Dongbang S, Kang C, et al. Disulfide- cleavage-triggered chemosensors and their biological applications. *Chem Rev* 2013;**113**:5071−109.
34. Schafer FQ, Buettner GR. Redox environment of the cell as viewed through the redox state of the glutathione disulfide/glutathione couple. *Free Radical Biol Med* 2001;**30**:1191−212.
35. Hu M, Furukawa S, Ohtani R, Sukegawa H, Nemoto Y, Reboul J, et al. Synthesis of prussian blue nanoparticles with a hollow interior by controlled chemical etching. *Angew Chem Int Ed Engl* 2012;**51**:984−8.
36. Buser HJ, Schwarzenbach D, Petter W, Ludi A. The crystal structure of prussian blue: $Fe_4[Fe(CN)_6]_3 \cdot xH_2O$. *Inorg Chem* 1977;**16**:2704−10.
37. Busquets MA, Estelrich J. Prussian blue nanoparticles: synthesis, surface modification, and biomedical applications. *Drug Discov Today* 2020;**25**:1431−43.
38. Liu Z, Liu J, Wang R, Du Y, Ren J, Qu X. An efficient nano-based theranostic system for multi-modal imaging-guided photothermal sterilization in gastrointestinal tract. *Biomaterials* 2015;**56**:206−18.
39. Zhu W, Gao M, Zhu Q, Chi B, Zeng L, Hu J, et al. Monodispersed plasmonic prussian blue nanoparticles for zero-background SERS/MRI-guided phototherapy. *Nanoscale* 2020;**6**:3292−301.
40. Wang Y, Pang X, Wang J, Chen Y, Song Y, Sun Q, et al. Magnetically-targeted and near infrared fluorescence/magnetic resonance/photoacoustic imaging-guided combinational anti-tumor phototherapy based on polydopamine-capped magnetic prussian bluenanoparticles. *J Mater Chem* 2018;**6**:2460−73.
41. Lv S, Miao Y, Liu D, Song F. Recent development of photothermal agents (PTAs) based on small organic molecular dyes. *Chembiochem* 2020;**21**:2098−110.
42. Song X, Gong H, Liu T, Cheng L, Wang C, Sun X, et al. J-Aggregates of organic dye molecules complexed with iron oxide nanoparticles for imaging-guided photothermal therapy under 915 nm light. *Small* 2014;**10**:4362−70.
43. Zheng M, Yue C, Ma Y, Gong P, Zhao P, Zheng C, et al. Single-step assembly of DOX/ICG loaded lipid-polymer nanoparticles for highly effective chemo-photothermal combination therapy. *ACS Nano* 2013;**7**:2056−67.
44. Fernandes N, Rodrigues C, Moreira A, Corrria IJ. Overview of the application of inorganic nanomaterials in cancer photothermal therapy. *Biomater Sci* 2020;**8**:2990−3020.
45. Song X, Wang X, Yu S, Cao J, Li S, Li J, et al. Co_9Se_8 Nanoplates as a new theranostic platform for photoacoustic/magnetic resonance dual-modal-imaging-guided chemo-photothermal combination therapy. *Adv Mater* 2015;**27**:3285−91.
46. Shao J, Xie H, Huang H, Li Z, Sun Z, Xu Y, et al. Biodegradable black phosphorus-based nanospheres for *in vivo* photothermal cancer therapy. *Nat Commun* 2016;**7**:12967.
47. Cheng L, Liu J, Gu X, Gong H, Shi X, Liu T, et al. PEGylated WS_2 nanosheets as a multifunctional theranostic agent for *in vivo* dual-modal CT/photoacoustic imaging guided photothermal therapy. *Adv Mater* 2014;**26**:1886−93.

48. Yavuz MS, Cheng Y, Chen J, Cobley CM, Zhang Q, Rycenga M, et al. Gold nanocages covered by smart polymers for controlled release with near-infrared light. *Nat Mater* 2009;**8**:935−9.
49. Liang X, Deng Z, Jing L, Li X, Dai Z, Li C, et al. Prussian blue nanoparticles operate as a contrast agent for enhanced photoacoustic imaging. *Chem Commun* 2013;**49**:11029−31.
50. Cheng L, Gong H, Zhu W, Liu J, Wang X, Liu G, et al. PEGylated prussian blue nanocubes as a theranostic agent for simultaneous cancer imaging and photothermal therapy. *Biomaterials* 2014;**35**: 9844−52.
51. Zhu W, Liu K, Sun X, Wang X, Li Y, Cheng L, et al. Mn^{2+}-doped prussian blue nanocubes for bimodal imaging and photothermal therapy with enhanced performance. *ACS Appl Mater Interfaces* 2015;**7**:11575−82.
52. Guo C, Jin Y, Dai Z. Multifunctional ultrasound contrast agents for imaging guided photothermal therapy. *Bioconjugate Chem* 2014;**25**:840−54.
53. Peng J, Dong M, Ran B, Li W, Hao Y, Yang Q, et al. "One-for-All" -type, biodegradable prussian blue/manganese dioxide hybrid nanocrystal for trimodal imaging-guided photothermal therapy and oxygen regulation of breast cancer. *ACS Appl Mater Interfaces* 2017;**9**:13875.
54. Fu J, Wu B, Wei M, Huang Y, Zhou Y, Zhang Q, et al. Prussian blue nanosphere-embeddedin situhydrogel for photothermal therapy byperitumoral administration. *Acta Pharm Sin B* 2019;**9**:604−14.
55. Overchuk M, Zheng G. Overcoming obstacles in the tumor microenvironment: recent advancements in nanoparticle delivery for cancer theranostics. *Biomaterials* 2018;**156**:217−37.
56. Parodi A, Quattrocchi N, Van de Ven A, Chiappini C, Evangelopoulos M, Martinez J, et al. Synthetic nanoparticles functionalized with biomimetic leukocyte membranes possess cell-like functions. *Nat Nanotechnol* 2013;**8**:61−8.
57. Liu Y, Wang Z, Liu Y, Zhu G, Jacobson O, Fu X, et al. Suppressing nanoparticle-mononuclear phagocyte system interactions of two-dimensional gold nanorings for improved tumor accumulation and photothermal ablation of tumors. *ACS Nano* 2017;**11**:10539−48.
58. García K, Zarschler K, Barbaro L, Barreto J, Malley WO, Spiccia L, et al. Zwitterionic-coated "stealth" nanoparticles for biomedical applications: recent advances in countering biomolecular corona formation and uptake by the mononuclear phagocyte system. *Small* 2014;**10**:2516−29.
59. Danhier F, Le Breton A, Preat V. RGD-based strategies to target alpha(v)beta(3) integrin in cancer therapy and diagnosis. *Mol Pharm* 2012;**9**:2961−73.
60. Xing F, Zhou C, Hui D, Du C, Wu L, Wang L, et al. Hyaluronic acid as a bioactive component for bone tissue regeneration: fabrication, modification, properties, and biological functions. *Nanotechnol Rev* 2020;**9**:1059−79.
61. Ungelenk S, Moayed F, Ho CT, Grousl T, Scharf A, Mashaghi A, et al. Small heat shock proteins sequester misfolding proteins in near-native conformation for cellular protection and efficient refolding. *Nat Commun* 2016;**7**:13673−87.
62. An Z, Tang W, Wu M, Jiao Z, Stucky GD. Hetero functional polymers and core-shell nanoparticles cascade aminolysis/michael addition and alkyne-azide click reaction of RAFT polymers. *Chem Commun* 2008; **48**:6501−3.
63. Liu T, Liu S. Responsive polymers-based dual fluorescent chemosensors for Zn^{2+} ions and temperatures working in purely aqueous media. *Anal Chem* 2011;**83**:2775−85.
64. Lai JT, Filla D, Shea R. Functional polymers from novel carboxyl-terminated trithiocarbonates as highly efficient RAFT agents. *Macromolecules* 2002;**35**:6754−6.
65. Li Z, Hu Y, Jiang T, Howard KA, Li Y, Fan X, et al. Human-serum-albumin-coated prussian blue nanoparticles as pH-/thermotriggered drug-delivery vehicles for cancer thermochemotherapy. *Part Part Syst Char* 2016;**33**:53−62.
66. Koppolu B, Zaharoff DA. The effect of antigen encapsulation in chitosan particles on uptake, activation and presentation by antigen presenting cells. *Biomaterials* 2013;**34**:2359−69.
67. Getts D, Martin A, McCarthy D, Terry R, Hunter Z, Yap W, et al. Microparticles bearing encephalitogenic peptides induce T-cell tolerance and ameliorate experimental autoimmune encephalomyelitis. *Nat Biotechnol* 2012;**30**:1217−24.
68. Yu G, Yang Z, Fu X, Yung BC, Yang J, Mao Z, et al. Polyrotaxane-based supramolecular theranostics. *Nat Commun* 2018;**9**:766.
69. Yang K, Liu Y, Zhang Q, Kong C, Yi C, Zhou Z, et al. Cooperative assembly of magneto-nanovesicles with tunable wall thickness and permeability for MRI-guided drug delivery. *J Am Chem Soc* 2018;**140**:4666−77.
70. Hsiang YH, Hertzberg R, Hecht S, Liu L. Camptothecin induces protein-linked DNA breaks mammalian DNA topoisomerase I. *J Biol Chem* 1985;**260**:14873−8.
71. Zimmer A, Amar-Farkash S, Danon T, Alon U. Dynamic proteomics reveals bimodal protein dynamics of cancer cells in response to HSP90 inhibitor. *BMC Syst Biol* 2017;**11**:33.
72. Rowe TC, Couto E, Kroll DJ. Camptothecin inhibits HSP70 heat-shock transcription and induces DNA strand breaks in HSP70 genes in *Drosophila*. *NCI Monogr* 1987;**4**:49−53.
73. Paduch R, Jakubowicz-Gil J, Niedziela P. Hepatocyte growth factor (HGF), heat shock proteins (HSPs) and multidrug resistance protein (MRP) expression in co-culture of colon tumor spheroids with normal cells after incubation with interleukin-1beta (IL-1beta) and/or camptothecin (CPT-11). *Indian J Exp Biol* 2010;**48**:354−64.
74. Liu S, Yuan Y, Okumura Y, Shinkai N, Yamauchi H. Camptothecin disrupts androgen receptor signaling and suppresses prostate cancer cell growth. *Biochem Bioph Res Co* 2010;**394**:297−302.
75. Elmallah M, Gordonnier M, Vautrot V, Chanteloup G, Garrido C, Gobbo J. Membrane-anchored heat-shock protein 70 (Hsp70) in cancer. *Cancer Let* 2020;**469**:134−41.
76. Yue X, Zhang Q, Dai Z. Near-infrared light-activatable polymeric nanoformulations for combined therapy and imaging of cancer. *Adv Drug Deliv Rev* 2017;**115**:155−70.
77. Zhang L, Zhang Y, Xue Y, Wu Y, Wang Q, Xue L, et al. Transforming weakness into strength: photothermal-therapy-induced inflammation enhanced cytopharmaceutical chemotherapy as a combination anticancer treatment. *Adv Mater* 2019;**31**:1805936.
78. Han R, Xiao Y, Yang Q, Pan M, Hao Y, He X, et al. Ag_2S nanoparticle-mediated multiple ablations reinvigorates the immune response for enhanced cancer photo-immunotherapy. *Biomaterials* 2012;**264**:120451.